Dynamics of edge localised modes in the TCV tokamak

A W Degeling, Y R Martin, P E Bak, J B Lister, X Llobet

Centre de Recherches en Physique des Plasmas, Association EURATOM-Confédération Suisse, Ecole Polytechnique Fédérale de Lausanne, 1015 Lausanne, Switzerland.

Abstract

The D_α emission time-series from the TCV tokamak was investigated for a large set of ELMy discharges, to determine whether fluctuations in the time delay between ELMs are the result of noise only, or whether a deterministic process in a chaotic state exists, as suggested by results on JT-60U [1]. This study was carried out by searching the time-series of each discharge for transient sequences that are generic to chaotic systems, called Unstable Periodic Orbits (UPOs). By taking a statistical approach, a subset of discharges with q95 greater than 2.6 were shown to contain many more UPOs than could be expected if dynamical system was noise dominated, and the properties of these UPOs were found to exhibit systematic variations with plasma parameters. Specifically, the period of the unstable fixed point ΔT^* was found to scale independently with the plasma current, density and the inner plasma – wall distance. In a number of cases, two separate fixed points were found to co-exist during the same discharge.

1. Introduction

It has been known for many years since the first demonstration on the ASDEX tokamak [2] that tokamak plasmas can undergo a sudden transition in the energy confinement time which is generally accompanied by a reduction in the deuterium visible light emission (D_α) and is referred to as the H-Mode [3]. The H-mode is frequently accompanied by bursts in MagnetoHydroDynamic (MHD) activity and in the D_α emission, known as Edge Localised Modes (ELMs) and this type of H-mode is referred to as the ELMy H-Mode. If ELMs do not appear, then the density usually rises uncontrollably, sometimes leading to a disruption. ELMs are most easily detected as spikes in the D_α signal, corresponding to a sudden increase in the line-of-sight integral of the ionisation rate in the plasma edge, which is concurrent with the abrupt, momentary disappearance of the H-mode transport barrier. ELMs are therefore assumed to play a role in stabilising the MHD conditions of the edge plasma by periodically releasing energy, which is typically in the order of a few percent (up to 10%) of the total plasma energy per ELM event. The triggering of an ELM is usually considered to arise from either: directly exceeding the ballooning limit [4], or by the coupling of ballooning modes to a low toroidal mode number kink-like instability [5], or to peeling modes [6]. Generally ideal ballooning modes are associated with type I ELMs and resistive ballooning modes with type III ELMs.

On large tokamaks, the release of a significant amount of energy in a sudden pulse with each ELM can cause surface damage to the first wall, especially the divertor plate. Very large ELMs would pose a huge problem for ITER for this reason. On the other hand, the periodic degradation in plasma confinement caused by an ELM is considered to be a plausible way of removing impurities and helium ash from a working reactor, so the complete absence of ELMs would not be acceptable either. As with all such necessary evils, it is clear that some level of control over the occurrence of ELMs is required, so that the largest and most destructive ELMs are avoided, while at the same time some level of particle and pressure control is maintained.

The TCV tokamak (conventional machine parameters: $R = 0.88$ m, $a \leq 0.25$ m, $B_T \leq 1.5$ T, $\kappa \leq 3$; discharge parameters achieved: $I_p \leq 1$ MA, $-0.7 \leq \delta \leq 1$, $1 \leq \kappa \leq 2.8$, $\langle n_e \rangle \leq 2.2\times10^{20}$ m^{-3}) [7] regularly obtains the H-mode in Ohmic conditions, both ELMy and ELM-free, with

limited and diverted plasmas [8]. The conditions for accessing and maintaining the H-Mode are presently being studied on many tokamaks, including TCV [9].

Many different types of ELM behaviour have been seen, summarised in [8]. The classification of ELMs in TCV as either Type I or Type III (according to the conventional scaling of average ELM frequency with the input power), is difficult because the input power cannot be scanned as an independent parameter in TCV ohmic H-modes. Figure 1 illustrates a small set of ELM sequences from TCV, identified by the D_α light seen on a vertically viewing central chord. In the top example, the ELMs appear in bursts with occasional ELM-free periods, caused by slight variations in the configuration [10]. In the second example, the ELMs appear to occur in pairs in a quasi-regular sequence. In the third case, the ELM activity appears to be irregular. There is often a correlation between the ELM amplitude, related to the pulsed energy release, and the time interval preceding the next ELM, a large delay leading to a larger burst of D_α light. Figure 2 illustrates this for TCV. In particular, this figure shows that a short inter-ELM delay was never followed by a large ELM amplitude, as evidenced by the empty space above the diagonal. It is therefore expected that controlling the time interval between ELMs should also affect the ELM amplitude distribution and that avoiding a long interval should reduce the possibility of obtaining excessively destructive ELMs.

Recently, ELM data from the JT-60U tokamak was examined [1] and preliminary observations made earlier on the JET tokamak [11] were confirmed, indicating that the ELM intervals are not randomly distributed about a mean value. The ELM occurrences exhibited behaviour that is characteristic of the deterministic evolution of a low-order non-linear dynamical system in a chaotic state. In particular, the ELM time series contained a specific type of short sequence known as an Unstable Periodic Orbit (UPO). This result opens the door to a new way of characterising the dynamics of ELMs, and also is extremely encouraging from the point of view of controlling the ELM amplitudes by controlling the ELM period.

The aim of the work described in this paper is to apply a similar approach to ELM time-series data from the TCV tokamak. We extend the previous work by analysing a large number of ELMy H-mode discharges for occurrences of UPOs and evaluate the statistical significance of the results. Further, we seek to establish how the properties of UPOs found vary with plasma parameters, and thereby point the way to establishing the necessary requirements for candidate models of ELM dynamics. The remainder of the paper is structured as follows. Section 2 presents the raw measurements and the analysis techniques. In this section we examine the inter-ELM intervals for all ELMy H-mode discharges and find that UPO

sequences occur much more frequently than could be expected if variations in the inter-ELM interval are random, confirming and generalising the earlier results from JET and JT-60U. We also examine the statistical distribution of UPO properties found in the data, and find that the UPOs may be divided into two sets. One set has a distribution consistent with so called "fake UPOs" that fit the selection criteria for a UPO simply by chance, and are accidental occurrences due to noise, while the other set shows reoccurrence properties that are expected for UPOs arising from a low order dynamical system with specific properties. By rejecting the former set we are able to extend previous work by exploring the properties of the underlying dynamical system revealed by the UPOs in Section 3. The location of the chaotic regime in the operational domain is characterised by the plasma parameter values at the time of occurrence of each UPO, and indications of systematic dependence of the UPO properties with key plasma parameters are found. Section 4 discusses the properties required of a model capable of reproducing these observations and the possibilities of subsequently controlling the ELM dynamics. Use is made of graphical representational techniques that are common when studying non-linear dynamical systems. As this methodology is relatively new to this field, some time is taken to explain the approach, and some technical details are given in Appendix A.

2. The search for chaos in ELM time-series

The repetitive occurrences of ELMs strongly suggest the existence of a cyclic dynamical system or relaxation oscillator. This system could involve the build up of a free energy parameter (such as the edge pressure gradient) to the threshold for an instability (the 'Edge Localised Mode', which in turn affects the transport, producing a spike in D_α emission), the onset of which 'relaxes' the system to a lower energy state (by rapidly deceasing the pressure gradient), whereupon the cycle repeats. A number of models of the ELM cycle as a dynamical system exist, and are reviewed in [12]. The analysis contained in this paper proceeds with this concept of the ELM cycle in mind: the cyclic process giving rise to ELMs may be described as a dynamical system, expressed by a limited number of ordinary differential equations. The observed D_α emission reflects the time variation in one, or a combination of the dependent variables of the dynamical system.

2.1. Generic behaviour of low order non-linear dynamical systems

This section briefly describes what an unstable periodic orbit is, which is required information for understanding the rest of the paper. Interested readers are referred to Appendix A and the

references therein for a more detailed discussion of some of the relevant features of chaotic dynamical systems.

Consider the general class of dissipative, non-linear dynamical systems with three dependent variables $\mathbf{x} = (x, y, z)$ such that $\dot{\mathbf{x}} = f(\mathbf{x}, \mathbf{a})$ (where f is a set of non-linear equations in $\mathbf{x}$, and $\mathbf{a}$ is a set of constants), which have periodic solutions with period τ_k: $\mathbf{x_k} = \mathbf{p_k}(t) = \mathbf{p_k}(t+\tau_k)$. In principle, the stability of these solutions can be found by standard perturbation analysis, which to first order, reduces to an eigenvalue problem for the perturbed quantities. For a periodic solution in three dimensions, the stability is given by the real parts of two eigenvalues (λ_1 and λ_2). If $\mathrm{Re}(\lambda) < 0$ for both the λ's, then the perturbation exponentially decays, and the solution is stable. If there is one λ for which $\mathrm{Re}(\lambda) > 0$, then the perturbation exponentially grows in the direction of the corresponding eigenvector, hence the solution is unstable. The existence and stability of the periodic solutions depends on the values of the constants **a**. If the values of **a** are such that all existing periodic solutions are unstable then the dynamical system is in a chaotic state, and $\mathbf{x}(t)$ may be bounded, but is never exactly periodic. Occasionally, $\mathbf{x}(t)$ in a chaotic system closely approaches one of the unstable periodic solutions $\mathbf{p}_k$ for which there is one positive and one negative eigenvalue (λ_+ and λ_-). When this happens, the behaviour of $\mathbf{x}$ is briefly described by the first order perturbed system, initially with exponential decay towards $\mathbf{p}$ according λ_- and subsequently exponential growth away from $\mathbf{p}$ according to λ_+. This transient behaviour is known as an unstable periodic orbit (UPO) and is generic to all chaotic systems.

2.2. Methodology: Finding Unstable Periodic Orbits in ELM Dynamics

To experimentally observe an unstable periodic orbit, one might expect that measurements of all of the dependent variables that make up the phase space of the dynamical system would be required, however this is not the case. Evidence of a UPO is also carried by the variations of consecutive periods ΔT_i of each of the dependent variables, therefore the time-series of a single diagnostic that contains information on at least one of the dependent variables will suffice, which, in the present case of studying ELMs is the D_α signal. In this case, the UPO is characterised by a short sequence of consecutive ΔT's (i.e. ΔT_i, ΔT_{i+1}, ΔT_{i+2}, …) that, for reasons explained in Appendix A, alternate above and below the value ΔT^* (the period of an unstable solution, called an unstable fixed point). The amplitude of the oscillation $|\Delta T - \Delta T^*|$ decreases exponentially during the approach phase of the UPO, and increases exponentially during the departure phase.

Figure 1d) illustrates an expanded view of a short sequence of ELMs seen on the D_α signal. This defines the inter-ELM period, based on a threshold detection scheme for determining the time of occurrence of an ELM, and the corresponding ELM amplitude. If the ELM with amplitude A_i occurs at the time t_i, then the inter-ELM period ΔT_i is defined by the time interval from this ELM to the next occurring ELM: $\Delta T_i = t_{i+1} - t_i$. Hence Figure 2 shows A_i versus ΔT_{i+1}. A signal containing ELMs is thereby reduced from a rapidly sampled time-series to a discrete set of inter-ELM periods defining a string of ELM events. Using these definitions, the evolution of the inter-ELM periods and amplitudes for a single discharge is shown in Figure 3.

Taking a large number of ELMs from a single discharge in essentially fixed conditions, we could use the probability distribution function of the inter-ELM period to provide a description of the ELM occurrences. This can be represented by a histogram of the central row of the data in the second row of Figure 3, as shown in Figure 4. Such a measure of the ELM occurrences might be expected to provide the only required description of the ELM time-series, and could be summarised by an average frequency and a random spread of given width around this frequency. The remainder of this section sets out to prove without doubt that this description is, in fact, inadequate to explain the experimental observations.

A particularly useful method of representing the sequence of inter-ELM time series is to create a scatter plot of all the consecutive periods ΔT_i against ΔT_{i+1}. The technical details of this so-called "first return map" are summarised in Appendix A, including an illustrative example. This technique is routinely employed in the study of non-linear dynamical systems governed by a limited set of ordinary differential equations (ODEs) in which periodic or chaotic behaviour is suspected, and has been very successful in distinguishing random behaviour from deterministic behaviour over a broad spectrum of fields [13]. This is because UPO signatures present in chaotic dynamics give rise to identifiable structures on the return map.

On the first return map, the transient approach and departure phases for a UPO appear as sets of consecutive points that follow straight lines, as shown in Figure 5. These straight lines are a direct result of the exponential decay and subsequent growth in $|\Delta T - \Delta T^*|$. Assuming that $|\Delta T - \Delta T^*| << \Delta T^*$, it is simple to show that the slopes (s_+ and s_-) of these lines are approximately related to the rate constants of the exponentials (the eigenvalues to the linearised system λ_+ and λ_-) by $|s_{+,-}| \approx \exp(\lambda_{+,-}\Delta T^*)$. These straight lines intersect one another on the diagonal of

the return map at the unstable fixed point (ΔT^*,ΔT^*), indicating the decay and subsequent growth in the variations of ΔT from the periodicity of the unstable equilibrium. As shown in the figure, the alternation of consecutive ΔT's about ΔT^* causes s_+ and s_- to be less than zero, since the y co-ordinate of each point becomes the x co-ordinate of the following point.

In our data, the approach phase of a UPO is much shorter lived than the departure phase, and is under-sampled on the return map. This has been found empirically to be the general case for the majority of dynamical systems. An illustration of why this should be the case in a chaotic system is given in Appendix A. Hence the slope during the approach phase (s_-) may only be roughly estimated once the departure phase and fixed point have been established. Since s_- is poorly determined in our data, it will not be used in any of the analysis presented in this paper.

Our initial task is to identify sequences of points on the return map of inter-ELM periods that fit the signature described above. We have used the following selection rules to identify UPO events in the data, which are applied in the order given.

1) Departure phase: The occurrence of at least three consecutive collinear points ((ΔT_i, ΔT_{i+1}), (ΔT_{i+1}, ΔT_{i+2}) (ΔT_{i+2}, ΔT_{i+3}), linear regression coefficient > 0.98) with a slope (s_+) less than −1 (i.e. $s_+ < 0$ to ensure alternation about ΔT^*, and $|s_+| > 1$ for exp. growth) . The candidate fixed point ΔT^* is obtained by intersection of the line of best fit from these points with the diagonal).
2) Approach phase: The slope of the line connecting the fixed point (ΔT^*,ΔT^*) with the point (ΔT_{i-1}, ΔT_i) must have a slope (s_-) between 0 and −1. The point (ΔT_{i-1}, ΔT_i) must also be on the other side of the diagonal to the point (ΔT_i, ΔT_{i+1}).

Figure 6 shows the first return map for all of the ELMs in a single TCV discharge with almost stationary conditions. Five sequences satisfy the above criteria during this discharge with three collinear points in the departure phase, and two sequences which have similar ΔT^* and s_+ values are shown in the figure. An expanded view of the time-series data showing the individual ELMs that comprise the sequences in each case and ELM periods as a function of time is shown in Figure 7a) and b) respectively. The corresponding candidate fixed points (ΔT^*) and the exponential divergence of the ELM period from the fixed point (the growth rate λ_+ was obtained by a least squares fit to $\log|\Delta T - \Delta T^*|$ for these plots) are shown on the plots by

dashed lines. As expected, the dashed lines with the corresponding slopes on Figure 6 compare well with the lines connecting the sequences. The UPO signature is not at all obvious from the ELM time-series shown in the top of Figure 7 – even after locating it.

A large number of ELMy H-mode discharges were obtained during an experimental campaign focused on the determination of the operational domain boundaries of this regime. Even though no additional power was used in these experiments, the large number of scanned parameters makes the experimental results useful for the study of H-mode basic physics. Access to the ELMy regime was found to occur in a quite small, but robust, region of the operational domain, which we regard as a gateway to the ELMy H – mode as described in [9]. Once in this desired ELMy regime, the plasma sustained changes in shape, current, and density over much wider ranges, thus allowing stationary ELMy phases to be performed in a wide range of plasma conditions. A total of 241 TCV ELMy H-mode discharges with up to 400 ELMs per discharge were examined for sequences satisfying the above criteria, of which 143 discharges were found to contain 536 separate occurrences with at least 3 collinear points in the departure phase.

2.3. Caveat: Chance Occurrences in Noisy and Random Time-Series

It is possible for signals resembling UPOs to occur by chance in a randomly generated time-series (so called "fake UPOs"). Therefore no single UPO can be claimed as evidence of an unstable fixed point, or chaotic dynamics, and the sequences of points that pass the above criteria should only be regarded as UPO candidates. However, the statistical properties of real UPOs (such as the histogram distributions of ΔT^*, s_+ and s_-) produced by a chaotic system will differ significantly from those produced by a random system, because the UPOs in the chaotic case contain specific information about the dynamical system, whereas randomly occurring fake UPOs are only subject to the distribution of ΔT's. In many dynamical systems it is found that only a limited number of discrete fixed point values exist. The real UPOs should therefore feature multiple occurrences of these particular values, whereas UPOs from a randomly generated time-series should produce a broad distribution.

In the case of a chaotic system that is affected by noise, the number of signals resembling UPOs that occur by chance may increase, and some of the UPO signals caused by actual close encounters with a fixed point may be obscured or destroyed. If the system parameters are affected by noise, the fixed point values estimated from the UPOs will become spread because of actual movements of the fixed point (not simply our measurement of it). However,

their distribution will be more closely grouped than the random case as long as the noise level is not sufficient to dominate the system.

2.4. Statistical Tests for Chaotic Dynamics

We therefore set out to test the hypothesis that at least some of the observed UPO candidates are caused by actual close encounters with an unstable fixed point, and hence that the system is indeed chaotic. To do this, we consider the null hypothesis: that ELM dynamics are always random or noise dominated, and that all the observed UPO candidates are chance occurrences governed by the probability distribution function (PDF) of ΔT's. If this is the case, then no information is carried in the particular ordering of the ELM time-series. Any random re-ordering of a given time-series, called a surrogate set, should be equivalent to the original time-series and have the same probability of giving rise to a "fake UPO" with a particular ΔT^*, because the PDF of ΔT's is unchanged. There are a number of other ways to produce surrogate sets, however this method, which preserves the PDF by randomly re-ordering the series has been selected as the easiest method to implement and interpret [14].

One hundred such surrogate sets were generated for each of the 241 ELMy H-mode discharges and each was searched for UPO candidates using the same algorithm employed on the original data. Contrary to [1], we found a consistently non-zero and therefore significant number of sequences fitting the criteria for a UPO in the surrogate sets. We made a statistical test to see if the UPO candidates found in the experimental data are distinguishable from these occurrences in the surrogates. Every sequence of points satisfying the criteria for a UPO that was found in the surrogates will be a fake UPO by definition [14], hence this set of fake UPOs defines the statistical properties expected for UPO candidates in the original data if the null hypothesis is true.

The most basic statistical test that gives a reliable, overall "yes or no" result is to compare the total number of UPO candidates found in all the ELMy H-mode discharges (N_{exp}) with the distribution of the total number of fake UPOs found in the surrogates (N_s, with mean value $\langle N_s \rangle$ and standard deviation σ_s), as shown in the top row of Table 1. The uncertainty in N_{exp} (given by $\sqrt{N}$) is small, and $\langle N_s \rangle$ is sufficiently large for the distribution of N_s to be approximated by a Gaussian. A useful figure of merit for comparing N_{exp} and $\langle N_s \rangle$ is the statistical significance K (also shown in Table 1), defined by:

$$K = \frac{N_{exp} - \langle N_s \rangle}{\sigma_s} \quad (1)$$

A value of $K \geq 3$ implies that the chances of all N_{exp} UPO candidates found in the original data being the product of a random process is less than 1%. The value of K for all discharges shown in the top row of Table 1 is much larger than 3, and therefore clearly indicates that, overall, many more UPO candidates occur in the experimental data than could be expected if the ELM time-series were produced by a random process, hence we reject the null hypothesis. Despite finding sequences resembling UPOs in the surrogates, we are thus able to confirm the existence of UPOs in the experimental data, demonstrating without doubt a deterministic process.

	No. of discharges	N_{exp}	$\langle N_s \rangle$	σ_s	K	P	$P.N_{exp}$
Figure 9a. (All data)	241	536	393.3	16	8.9	0.27	145
Figure 9b. (Filtered data)	39	168	9.95	3.36	47	0.94	158
Figure 9c. (All data – filtered data)	202	368	383.5	15.5	-1	-0.042	-

Table 1 : Statistics for the comparison of UPO candidates from the experiment against those found in the surrogate sets. Column definitions are: No. of discharges: number of discharges that contain UPOs candidates; N_{exp}: Total number of UPOs; $\langle N_s \rangle$: the mean value of the number of fake UPOs (N_s) in the 100 surrogate sets; σ_s: Standard deviation of N_s; K: Statistical significance (equation (1)); P: Probability that any one UPO candidate is real (equation (2)); $P.N_{exp}$: Estimation of the total number of real UPOs from the product of P and N_{exp}.

Finding a significant number of fake UPOs in the surrogates implies it is almost certain that a number of the UPO candidates found in the experimental data are chance occurrences. A crude measure of the probability P that any one of the UPO candidates (that contribute to N_{exp}) is *not* a chance occurrence, and hence indicates an unstable fixed point, is given by:

$$P = 1 - \frac{\langle N_s \rangle}{N_{\exp}} \tag{2}$$

Roughly 27% of the 536 UPO candidates found, an as yet undefined subset of about 145 elements, are therefore likely to be the result of actual close encounters with an unstable fixed point.

A more detailed statistical test is to compare the number of UPO candidates in each discharge (called n_{shot}) with the distribution of the number of fake UPOs in the corresponding surrogate sets of that discharge (n_s). For a small number of discharges that were used as test cases, 10^4 surrogate sets were generated, and it was found that the distribution of n_s closely resembles a Poisson distribution $p_\mu(x)$:

$$p_\mu(x) = e^{-\mu} \frac{\mu^x}{x!} \tag{3}$$

where x is the number counts per set and μ is the mean value of x in the limit as the number of sets becomes large. This is the expected result for a random process with a large number of 'trials' (i.e. the number of points in each surrogate set) and a small 'success' probability per trial (i.e. the probability of producing a fake UPO) [15]. The probability of finding n_{shot} UPO candidates in a single discharge if a random process is operating may therefore be estimated by:

$$p_{\langle n_s \rangle}(n_{shot}) = e^{-\langle n_s \rangle} \frac{\langle n_s \rangle^{n_{shot}}}{n_{shot}!} \tag{4}$$

In principle, this should allow an estimation to be made on a discharge to discharge basis of the likelihood that a random or chaotic process is operating. Figure 8 shows $p_{\langle n_s \rangle}(n_{shot})$ evaluated as a function of n_{shot} for each discharge where $n_{shot} > \langle n_s \rangle$, and shows that a subset of 13 discharges containing more than 10 UPO candidates per discharge have less than 1% probability of being the product of a random process, hence they may safely be labelled chaotic. There is a large collection of discharges with fewer than 10 UPO candidates per discharge, some of which also have $p_{\langle n_s \rangle}(n_{shot})$ less than 1%, however the statistical uncertainty in n_{shot} (i.e. $\sqrt{n_{shot}}$) is no longer negligible, and prevents any clear classification by this method.

2.5. Enriching the Database for "Real" UPOs

The first row of Table 1 shows that only about 27% of the 536 UPO candidates are likely to be the result of an actual close encounter with an unstable fixed point (so called "real" UPOs). Examining the number of UPOs on a discharge to discharge basis has indicated a small number of discharges that are definitely chaotic, however there is no guarantee that all the UPO candidates in these discharges are real, nor that all of the candidates in the other discharges are necessarily fake. In this section we attempt to filter the database of UPO candidates to increase the proportion of real UPOs to fake UPOs, so that a meaningful investigation of the locations and properties of the associated unstable fixed points as functions of the plasma parameters may be carried out later.

To accomplish this, we make a closer examination of the properties of UPO candidates from both the experimental data and surrogate sets. Each UPO candidate has the following measurable parameters: ΔT^*, λ_+, λ_-, ε (the point of closest approach to ΔT^*) and R (the linear correlation coefficient for the departure phase). Multiple candidates from the same discharge also have δT (the absolute difference in period between a candidate fixed point and its nearest neighbour) and δs (the absolute difference in s_+ for the same pair). These parameters were histogramed for all candidate UPOs in the real and surrogate sets using a logarithmic scale for the bins, and the resulting distributions were examined. The distributions for δT and δs are shown in Figure 9a) (solid curves with circles) and the remainder are found in Appendix B of [16]. For the surrogates, the distribution of mean values (solid curve with crosses) and the mean plus and minus 3 standard deviations (upper and lower solid curves) are displayed. These curves show that in each case a range of values exist where the distribution for the experimental data shows a significant peak that lies above three standard deviations of the mean of the surrogate distribution, while elsewhere the distributions are largely similar. These peaks are the result of the distributions of the experimental data having a different shape to the surrogate distributions (i.e. their moments are significantly different).

The peaks in the distributions for δT and δs both become well separated from the mean of the surrogate distributions as δT and δs are decreased, representing a subset of UPOs with properties that are more closely grouped than the others. Such grouping may be produced by multiple re-occurrences during each discharge of a limited number of unstable fixed points in the underlying dynamical system. Hence, these peaks in δT and δs are most likely to be the result of the subset of real UPOs lying within the set of UPO candidates.

Therefore a filter was devised to examine the clustering properties of UPO candidates in the experimental data, by keeping only those pairs of candidates occurring in the same discharge that have $\delta T < 0.05$ ms and $\delta s < 0.5$ (indicated by vertical dotted lines in Figure 9). This corresponds to assuming that fake UPOs have a negligible probability of recurring with identical properties. As shown in the second row of Table 1, the number of UPO candidates that survive the filter is reduced to 168, and come from a subset of 39 discharges. The same filter was applied to the corresponding surrogate sets of this subset of discharges in order to apply the null hypothesis test. The average of the total number found in these surrogates after filtering is only 9.95. Hence the chances of any one of the UPO candidates that pass the filter from the experimental data being a random occurrence is now only about 6%. Figure 9b) shows the distributions of the surviving UPOs from the experimental data and surrogate sets for δT and δs (distributions of the other parameters are found in Appendix B of [16]). In each case, the peak in the distribution for the experimental data corresponds to the anomalous parts of the unfiltered distributions in Figure 9a), while the surrogate distributions have been almost totally removed. This demonstrates that a common set of UPO candidates with distinct properties gives rise to the anomalies in Figure 9a).

Figure 9c) shows the result of subtracting the filtered distributions for the real and surrogate data from the unfiltered data shown in Figure 9a). In each case, the resulting real and surrogate data have largely indistinguishable distributions, demonstrating the efficiency of the filter in removing candidate UPOs that are consistent with the null hypothesis, and keeping only the anomalies. This is also indicated by the values of K and P for these data shown in the third row of Table 1, which are both close to zero. If the filter retained too many (or too few) candidates then the distribution for the experimental data in Figure 9c) would lie significantly below (or above) distribution of the surrogates while the values of K and P would be larger in magnitude.

We are thus able to select a subset of the UPO candidates that are distinguishable from the rest of the candidates by their statistical properties, and are clearly not the result of a random process. We conclude that these signals are most likely to be the result of actual close encounters with unstable fixed points in the underlying dynamical system. This is a significant statistical test of the generality of the results of Bak [1]. A large number of discharges over a range of conditions, not just isolated examples, have been searched for features indicating determinism in ELM dynamics.

3. Effect of varying the tokamak discharge conditions

We have identified a set of UPOs that, we can say with a high degree of confidence, reflect the period of some of the unstable fixed points in the underlying dynamical system. In these discharges the level of noise must have been sufficiently low for the dynamical system in a chaotic state to be visible. This section focuses attention on the discharges where the system is clearly chaotic. In Section 3.1 we investigate the regimes in the operational domain of parameters where chaotic behaviour occurs, compared to the operational domain of the ELMy H-mode, and in Section 3.2 we investigate the variation of the unstable fixed point period ΔT^* in the chaotic regime as a function of various plasma parameters.

To facilitate this, a database was compiled for the set of UPOs that contains the values of around 50 plasma parameters obtained by various diagnostics and derived quantities during each TCV discharge, sampled at the time of closest approach for each UPO (referred to as the UPO database) . A database with the same parameters regularly sampled during the ELMy phases of H-mode discharges was also compiled (referred to as the "TCV H-mode database"), and used for comparisons in Section 3.1.

3.1. The Operational Domain of the Chaotic ELMy H-Mode

We attempt to identify a boundary defining the chaotic ELMy regime in the operational domain. Firstly, we need to identify the operational domain of the ELMy H-mode, indicated by the region in parameter space occupied by samples from the TCV H-mode database. Each sample represents a small time interval of typically 16 ms, so the density of these points weighted by their intervals indicates the total time spent in a given region of parameter space during the experimental campaign. Figure 10 shows a series of contour plots from the TCV H-mode database with all possible combinations of κ (plasma elongation), n_e (line integrated electron density in 10^{19} m^{-3}), Δ_{in} (minimum radial plasma-wall distance, or 'GAPIN' in mm), I_p (plasma current in kA) and q_{95} (q at the flux surface enclosing 95% of the poloidal magnetic flux), as the x and y axes. The contour levels were computed by binning the points from the database using a 80×80 grid over the space shown in the figure, summing the corresponding sampling intervals associated with each point, and finally applying a boxcar average (i.e. convolution with a constant 5×5 matrix). Hence the light, medium and dark grey contour levels, drawn at values of 1, 10 and 100 ms per bin respectively, indicate the total time spent in each locality of parameter space defined by the position and dimensions of each bin. In these experiments, parameter scans were made in I_P, κ, n_e and Δ_{in}, starting in each case

from a range of values that were used as standard conditions, located close to the gateway for entry to the H-mode in the TCV operational domain [9]. This region corresponds to the most frequently sampled location in each projection of the operational domain shown in Figure 10, and consistently gave rise to discharges with a long, stationary ELMy H-mode phase. Parameter scans are indicated in these plots by limbs of data extending away from this region. The small crosses also shown on these plots mark the positions in parameter space of each UPO (i.e. the state of the plasma at each UPO event). Hence areas in parameters space where the density of crosses is high indicates approximate domains in parameter space which are shown to be chaotic.

This figure shows that, in projections of I_P, κ and n_n, the density of UPOs and the occupation time are both strongly peaked at the same location, at the standard conditions. Very few UPOs are found along the scans of these three parameters that extend away from the standard conditions. In contrast, the left-hand column of graphs show that a number of dense collections of UPOs occur at discrete values of Δ_{in}, which correspond to flat-top settings during a short series of discharges where Δ_{in} was scanned. The fourth row of graphs, with q_{95} as the y-axis, show that nearly all the UPOs occur with q_{95} values above 2.6, and that the occupancy time was high (i.e. over 100ms per bin) in each projection, over a range of q_{95} values from 2.3 to 2.8. These graphs also show that the parameter scans in I_P, κ, and n_e were made with $q_{95} < 2.6$, while the Δ_{in} scan was made with $q_{95} > 2.6$, suggesting that a threshold value of q_{95}, rather than the scanned parameters, was responsible for the observed presence or absence of UPOs.

The apparent "chaotic domain" above this threshold value in q_{95} should be interpreted as a domain where the noise level in the experiment was sufficiently low to allow the observation of chaotic dynamics – it does *not* necessarily represent a boundary between chaotic and non-chaotic regimes. A deterministic, non-chaotic regime (with a low level of noise) would be indicated by a set of discharges with a statistically significant *lack* of UPO candidates compared with their surrogates [14]. Our search for such a set has been inconclusive. There is a large group of discharges containing zero UPO candidates, however the mean number of fake UPOs found in their surrogates is too small (typically $\langle n_s \rangle \sim 1$) for these null results to be considered significant.

3.2. Unstable Fixed Point Dependence within the Chaotic Regime

In this section, variations of ΔT^* with the plasma parameters are investigated to search for any systematic behaviour. The general method of analysis was to choose a specific parameter, and remove points from the database that vary by more than a given tolerance in each of a number of other key parameters, defining a small multi-dimensional parameter window for examination. In so doing, the variation of ΔT^* with the parameter of interest in each case was estimated, keeping the other parameters roughly constant, within the tolerance in each parameter. This process presents a dilemma: ideally the parameter window should be made as small as possible to remove the effect of variations due to these other parameters, however the number of points remaining must be sufficient to describe some functional dependence, if it exists. Starting with 168 points in the UPO database, the density of points over the multi-dimensional domain of parameters is low, and evidence of structures revealed by this procedure, over and above a general trend, must be considered as a preliminary indication that such structures may exist. As such, this section reports preliminary results for parameter regimes that potentially show particularly interesting behaviour and warrant further detailed examination. The parameter windows used to produce Figure 11, Figure 12 and Figure 13 to be discussed in this section are given in Table 2, and show the variation in ΔT^* with I_P, Δ_{in}, and n_e respectively. The grey points in these figures are the inter-ELM periods (ΔT_{ELM} in the figures) from the TCV H-mode database from the same selected shots, for time samples that also fall within the parameter windows of Table 2. Parameter definitions used in this table and in the figures that have not yet been defined are: V_{surf}: Loop voltage at the plasma edge; θ_{SP} : poloidal angle of divertor leg strike point from magnetic axis; δ : plasma triangularity ; δ_L: lower plasma triangularity; L_{leg} : length of longest divertor leg ; V_{GR} : reference voltage for gas puffer.

Figure 11 shows the variation ΔT^* with I_p. Although the filtering process only leaves a sparse scattering of data points, a linear trend of ΔT^* with I_p is clearly evident over a wide range. This trend is also evident in the distribution of inter ELM periods, although the scatter is much larger. The discretisation of data in I_P is due to the single, constant current setting during the ELMy H-mode phase in each of the limited number of discharges used to produce the figure.

Figure 12 shows the variation of ΔT^* with the minimum radial gap between the plasma and the central column. Most of these points originate from a series of similar discharges (each

designated by a different symbol in the plot) in which the inner gap was scanned from discharge to discharge. Apart from a generally increasing trend of ΔT^* with Δ_{in}, this figure appears to show the development of two distinct fixed points as Δ_{in} is increased. Certainly no such distinction is visible for $\Delta_{in} < 0.01$ m. However, the group of points at $\Delta_{in} \approx 0.012$ m may be separable into two groups with three points occurring at $\Delta T^* \approx 3.95$ ms and the others spread between 3.8 and 3.5 ms, although it is true that the width of the latter group is larger than the separation between groups. The points at $\Delta_{in} \approx 0.017$ m are more clearly separable into two groups at $\Delta T^* \approx 4.25$ ms and 3.9 ms, and the two groups of points at $\Delta_{in} \approx 0.025$ m are also well separated. The inter ELM periods show no evidence of this separation, and only broadly reflect the increasing trend with Δ_{in}. As in Figure 11, the discretisation of data in Δ_{in} is due to the limited number of discharges used to produce the figure.

Figure 13a) shows the variation of ΔT^* with the plasma density for three cases, labelled Group A, B and C in the plot. These cases have the same window for κ, δ and strike-point, Group C (triangles) have a lower Δ_{in} than the others, and Group A (circles) have a longer divertor leg length than the others, as shown in the inset to the figure. As a whole, the figure shows a generally increasing trend of ΔT^* with n_e. The inter-ELM periods also show this trend, although the scatter is very high. Both the inter-ELM periods and ΔT^* show two principal groups of data at high and low densities, separated by a vacant region at about 7×10^{19} m^{-3}. This simply corresponds to the density levels chosen for the discharges used to produce this figure.

On closer inspection, indicated in Figure 13b), it may be argued again that in each case the data may be split into an upper and lower group in ΔT^*, with each group scaling linearly with n_e, as indicated by the dashed lines in the plot. Although only a sparse scattering of points make up each individual trend, the repetitions of very similar trends in these three cases make this argument more compelling.

Parameter.	Figure 11		Figure 12		Figure 13					
					Group A		Group B		Group C	
	Min.	Max.	Min.	Max.	Min.	Max.	Min.	Max.	Min.	Max.
q_{95}	—	2.75	—	—	—	—	—	—	—	—

V_{surf} [V]	*-1.4*	*-1.17*	—	—	—	*-1.18*	—	*-1.18*	—	*-1.18*
θ_{SP} [rad]	4.18	4.4	—	—	4.15	4.24	4.15	4.24	4.15	4.24
Δ_{in} [m]	0.0245	0.03	—	—	0.023	0.032	0.023	0.032	0.015	0.023
δ	—	—	—	—	0.565	0.626	0.565	0.626	0.565	0.626
δ_L	—	—	—	—	—	*0.796*	—	*0.796*	—	*0.796*
I_P [kA]	—	—	—	—	—	*408*	—	*408*	—	*408*
κ	—	—	1.7	1.75	1.7	1.75	1.7	1.75	1.7	1.75
L_{leg} [m]	—	—	0.131	0.22	0.19	—	0	0.19	—	—
n_e [10^{19} m^{-3}]	—	—	6.4	7.0	—	—	—	—	—	—
V_{GR} [V]	—	—	1.9	2.1	—	—	—	—	—	—

Table 2 : Parameter windows (minimum and maximum values) for filters applied to the UPO and TCV H-mode databases that produced Figure 11, Figure 12 and Figure 13. Parameter definitions are: q_{95} : q at the flux surface enclosing 95% of the poloidal magnetic flux; V_{surf}: Loop voltage at the plasma edge; θ_{SP} : poloidal angle of divertor leg strike point from magnetic axis; Δ_{in}: minimum radial plasma-wall distance, or 'GAPIN'; δ : plasma triangularity ; δ_L: lower plasma triangularity; I_p: plasma current; κ : plasma elongation ; L_{leg} : length of longest divertor leg ; n_e: line integrated electron density; V_{GR} : reference voltage for gas puffer.

Twelve points from Group C between densities of 6.5 and 6.9×10^{19} m^{-3} originate from a single discharge (discharges number 19219, also used in Figure 12), the time-series of ΔT's and corresponding return map of which are shown in Figure 14. The return map very clearly shows two distinct groups of UPOs, each with similar properties, indicating that they are multiple re-occurrences of the same two unstable fixed points (designated by a square and up-side-down triangle in the figure). The time-series also shows the occurrence time and fixed point values of the UPOs from these two groups with the same symbols. This plot shows that the average ELM frequency gradually increases during the first half of the discharge (attributed to a gradual decrease in Δ_{in} during this period), and that nearly all of the UPOs occur in the latter half, with the longer period fixed point occurring first. During the latter half

of the discharge, both the upper and lower unstable fixed points are encountered with no apparent order, strongly suggesting the simultaneous existence of both fixed points.

4. Discussion

Figure 11, Figure 12 and Figure 13 show trends that reflect well known scalings of the ELM interval with I_p, Δ_{in} and n_e. One might say that it should come as no surprise that these trends are found, since ΔT^* must lie within the distribution of ELM intervals. However, our interpretation of this result, based on the rejection of the null hypothesis in Section 2, is the reverse. The well known scalings of ELM interval with I_p, Δ_{in} and n_e are found *because* of movements of the unstable fixed points (ΔT^*) in the underlying dynamical system, which are caused by variations in these parameters. In this sense, the observed variations of ΔT^* with the plasma parameters (or at least, more detailed studies of this nature) should serve as a benchmark for candidate dynamical models of ELMs when in the chaotic regime. In principle, the boundary between chaotic and non-chaotic regimes found in dynamical models should also be verifiable experimentally. Our data give no result on this point simply because the duration of the ELMy H-mode phase with no UPOs did not give a statistically significant null result. The structure of unstable periodic orbits found experimentally, the number of approach and departure directions for an unstable fixed point, and the values of the associated exponential decay and growth, should also serve as features that must be reproduced in a successful model.

Unstable periodic orbits reflect topological features of the dynamical system, and provide insight into the form of differential (or difference) equations required in a successful model. Generally in chaotic dynamical systems, there are large families of unstable periodic orbits and associated fixed points, with increasing complexities. In this work we have searched for the simplest type of UPO, which appears as a transient phase of decay and subsequent exponential growth on the first return map. The fixed point is called a 'period 1 fixed point' because the UPO appears in the variation of consecutive periods. More complicated UPOs with 'period n' fixed points (where $n > 1$) may be found by searching for the same pattern on higher order return maps, where ΔT_i is plotted against ΔT_{i+n} . Recently it has been found that the way unstable periodic orbits interlink with one another is a fundamental characteristic of the dynamical system, and provides a means of modelling the dynamics of an experimental system once a small subset of the periodic orbits has been identified [17]. The work presented in this paper represents a small, first step in this direction, and gives some basic information

on the dynamical system. For example, the finding of two unstable fixed points in our data allows families of differential equations that have only a single, period one, unstable fixed point to be ruled out (such as the Rossler attractor described in Appendix A).

Over the last decade a number of techniques have been developed for controlling chaotic dynamical systems by means of small feedback corrections to a control parameter. These algorithms are designed to effectively stabilise an unstable periodic orbit in the unperturbed dynamical system, thereby obtaining regular behaviour by locking onto a desired fixed point. One way of doing this (the so called OGY method after Ott, Greborgi and Yorke [18]) is to configure the feedback algorithm to repeatedly provide a correction during a UPO that moves the state of the system from a point in phase space along the unstable direction to a point along the stable direction. The corrections only need to be small perturbations, because the system is close to equilibrium in the neighbourhood of the fixed point. Most importantly, it is not necessary to have prior analytical knowledge of the system dynamics to use this method.

The implication for the control of ELMs is by analogy with other chaotic systems. By choosing an unstable fixed point with a low ΔT^*, such control ought to be able to minimise the probability of a large ELM-interval and hence of a large ELM, due to the correlation between interval and ELM size. The results from Section 3.1 that fail to show any clear evidence of boundaries to the chaotic regime in the operational domain, with the exception of q_{95}, offers some encouragement to the general applicability of this method.

If this type of control algorithm is to be employed, a control parameter has to be identified which is capable of influencing the trajectory in the neighbourhood of the fixed point. Some parameters that influence the dynamics, such as elongation and density, would be unsuitable for controlling burning plasma ELMs. Others, such as manipulating the edge current directly using external current drive, might prove to be useful. Searching for the most suitable control variables to influence ELM dynamics and ultimately pave the way for active control is also the object of ongoing work on the TCV tokamak.

5. Conclusions

The hypothesis that the apparently random variations in the delay period between ELMs are in fact due to a deterministic chaotic process has been tested for all of the ELMy H-mode phases recorded on TCV. The time series of ELM intervals for each discharge was examined for short time-scale structures known as unstable periodic orbits, which are known to be signatures of chaotic dynamics, and indicate the periodicity of unstable solutions to the

dynamical system, known as unstable fixed points. We consider the possibility that signals resembling UPOs may occur by chance in a noise dominated system, and demonstrate that the results of our search are in clear disagreement with this null hypothesis. We thereby conclusively demonstrate the existence of chaotic dynamics. Further, by considering the statistical properties of signals resembling UPOs that occur by chance, we were able to apply a filter to the experimental data sets to remove such chance occurrences, leaving only those UPO signals, to a high degree of confidence, that truly indicate an unstable fixed point. Taking this filtered set of UPOs, we find in the cases of I_p, κ, n_e and Δ_{in} that the number of UPOs found appears to roughly correspond to the occupancy time, while a clear lack of UPOs are found for $q_{95} < 2.6$. This lack of UPOs is interpreted to indicate an increase in the noise level affecting the dynamical system, such that the system appears to be noise dominated below this value. Determining the boundaries of the chaotic regime clearly has implications on the prospects of controlling ELMs via a control algorithm based on UPOs. These results therefore offer some encouragement for ELM control by this method. Within the chaotic domain, the periodicity of unstable fixed points show systematic variations with the plasma parameters, and on a number of occasions, two unstable fixed points were found to exist. These observations, although preliminary, should serve as a benchmark for dynamical models of ELMs.

Acknowledgements: Thanks go to the TCV team without whom the experimental results would not be analysable. This work was stimulated by prior work on the JET and JT-60U tokamaks and the encouragement of Dr. R. Yoshino is gratefully recognised. One of the authors (PEB) wishes to thank the CRPP for financial support in Lausanne during this work, which was partly supported by the Swiss National Science Foundation**.** The authors especially thank L. Studer from Lausanne University for many helpful discussions.

Appendix A

The purpose of this appendix is to give a concise introduction to some of the concepts encountered when dealing with chaotic dynamical systems. Attention is focussed on issues pertaining to unstable periodic orbits that have arisen in the paper: 1) how the structure of UPOs can be understood in terms of the properties of chaotic dynamical systems, 2) how the stability of periodic solutions, or fixed points are found, and 3) how the UPO structure manifests itself on the return map, allowing its detection by the means described in Section 2.2. Interested readers are directed in particular to an excellent review by Gilmore [17], and to the textbooks [19], [20], [21], [22] for further information.

A chaotic system has two fundamental properties [17]:

1) Sensitivity to initial conditions.
2) Recurrent, non-periodic behaviour.

The first point means that any two sets of initial conditions that start arbitrarily close together will diverge from each other exponentially with time. Using a graphical analogy, where the state of the system as a function of time marks out a line, or trajectory in space, the trajectories starting at the two initial conditions are stretched apart. The second point means that the state of the system is bounded, hence these trajectories cannot continue diverging to infinity, but eventually reach a point of maximum separation before approaching one another again. This may be thought of as the trajectories being squeezed together again. We will restrict ourselves to considering dissipative dynamical systems, where such squeezing processes give rise to an attractor, as described in the following paragraphs.

A chaotic dynamical system may be expressed by a set of coupled first order non-linear, ordinary differential equations (ODEs) $\dot{\mathbf{x}} = f(\mathbf{x}, \mathbf{a})$, where $\mathbf{x}$ is a vector (length at least 3) of continuous time dependent variables and $\mathbf{a}$ is a set of constant parameters. A simple example of a system of ODEs that exhibit chaos is the Rössler equations [23]:

$$\begin{aligned} \dot{x} &= -(y+z) \\ \dot{y} &= x + \alpha y \\ \dot{z} &= \alpha + z(x-\mu) \end{aligned} \qquad (5)$$

where α and μ are constant parameters. It is a simple procedure to compute the trajectory of the state of this system as a function of time in the three dimensional space defined by {x,y,z} (phase space), as shown in Figure A.1a) (for α = 0.2 and μ = 4.6). This dynamical system is

dissipative, which means that the trajectory of the system in phase space must converge to an object with fewer dimensions than the space itself, called an attractor (i.e. an attractor in 3D phase space must have less than 3 dimensions). The object marked out by the trajectory is the so-called Rössler attractor. Chaotic attractors are also called 'strange' attractors because they have a fractal structure. The Rössler attractor appears for the most part to be a two dimensional sheet (except for the part of the attractor where trajectories pass over one another), with a hole in the middle of it. Close examination of the attractor however, shows it is comprised of an infinite succession of parallel layers compressed together. It has been shown that such structures have a non-integer dimension (called a fractal dimension), which, in the case of the Rössler attractor is slightly greater than 2. While the state of the system is clearly bound to the attractor in phase space, the trajectory is never exactly periodic – i.e. the trajectory is not a closed loop. Further, it is impossible to predict the long-term path of the trajectory on the attractor, since any two neighbouring initial conditions take exponentially diverging paths, so any non-zero imprecision in the calculation rapidly grows. In this sense the numerically computed trajectory cannot be considered accurate over a long period, although the shape of the attractor is accurate.

For low values of μ and α, the Rössler equations are found to support stable, perfectly periodic solutions – that is, non-chaotic behaviour. Some examples are shown in Figure A.1 b), c) and d). As described in Section 2.1, the stability of these solutions may be determined in principle by linear perturbation analysis. Each periodic solution is stable within a given domain of α and μ. As shown in the figure, increasing the value of μ above a threshold value causes a new stable periodic solution to be born from the old solution with roughly twice the path length, and a correspondingly longer period. The transition from the old solution to the new solution is called a period doubling bifurcation. The old solution still exists, however it is no longer stable. As μ is further increased, the new periodic solution remains stable until another threshold value for bifurcation is reached, at which point it too becomes unstable, and gives birth to another new solution with twice the period. This process of bifurcations continues with increasing μ, with the threshold values occurring closer and closer together until a saturation value is reached and all existing periodic solutions become unstable. This is the threshold for chaotic behaviour, and the above process is called the bifurcation route to chaos.

Chaotic Dynamics as a Cyclic Process

A qualitative understanding of a chaotic dynamical system comes down to determining the cyclic processes that give rise to the shape, or topology of the attractor. For example, the topology of the Rössler attractor may be understood by the following cycle of algorithmic steps [19]: a) take a plane rectangular sheet (i.e. a 2D surface); b) take one end and stretch it in the middle to make an up-side-down 'U' shape, and squeeze it together to make a fold, while leaving the other end unfolded and flat; c) join the two ends together to make a loop. In so doing, the folding process is continually iterated by the loop, producing an object with an infinite number of densely packed surfaces – the strange attractor.

The folding process described above for the Rössler attractor is a generic feature that may be found in a wide range of more complicated low order dynamical systems – for this reason the Rössler attractor has been described as the 'Hydrogen atom' of chaotic systems [17]. As such we shall use it as an example to illustrate how the existence of periodic solutions, and the generic features of unstable periodic orbits (enabling their detection) can be inferred from this picture of the dynamical system. In this section we thus examine the dynamical system in a chaotic state – that is all the periodic solutions are unstable. How the solutions become unstable is treated in the next section.

Recall from Section 2.1 that UPOs are characterised by the approach and subsequent departure of the state of the system from a periodic solution that is unstable, and are characterised by the eigenvalues λ_- and λ_+ (whose real parts are respectively less than and greater than zero). Figure A.2 shows a cross section of the end of the rectangular sheet undergoing four iterations of the cyclic stretching and squeezing process. In this diagram the squeeze is left incomplete to enable the build up of layers to be visualised. The position of the point marked by an 'x' in each diagram remains unchanged after each cycle, hence a trajectory that passes through (exactly) this point marks out a closed, periodic orbit in phase space. The filled dot also shown in each figure marks the evolution in position of an unstable periodic orbit on the sheet. Initially this point is well separated from the x. The combined effect of the first stretch and squeeze is to move the point to nearly the same position as the x. This is the approach phase of the UPO, and the direction of the squeeze is expressed by the eigenvector corresponding to λ_-. The next three iterations show that the separation between the point and the x increases, with the point alternating on either side of the x after each iteration. This corresponds to the departure phase of the UPO, with the eigenvector

corresponding to λ_+ expressing the direction of the stretch. The alternation of the UPO about the periodic solution is thus explained by the rotation by 180 degrees of the local surface of the sheet (the attractor), which is caused by each iteration of the folding process. This rotation is expressed by the imaginary parts of both eigenvalues having a value $\mathrm{Im}(\lambda_{+,-}) = \omega_o/2$, where ω_o is the fundamental frequency of the periodic solution ($2\pi/\Delta T^*$).

Evaluating the Stability of Periodic Solutions

Figure A.2 also illustrates how the cyclic iteration of stretching and squeezing processes can be thought of as a mapping, in which the initial conditions for one cycle ($\mathbf{x}_i$) are mapped by a non-linear transformation to produce the initial conditions for the next cycle ($\mathbf{x}_{i+1}$). An example of the result of such a mapping, called the Hénon map, with very similar properties to the Rössler attractor (i.e. the dynamical system it describes is subject to a similar stretching and squeezing process) is used to produce the four levels shown in Figure A.2. In this case the dynamical system is expressed as a set of difference equations:

$$\mathbf{x}_{i+1} = \mathbf{F}(\mathbf{x}_i, \mathbf{a}) = \begin{pmatrix} f(x_i, y_i) \\ g(x_i, y_i) \end{pmatrix} = \begin{pmatrix} y_i + 1 - ax_i^2 \\ bx_i \end{pmatrix} \text{ (for the Hénon map)} \qquad (6)$$

where the mapping functions **F** explicitly state the stretching and squeezing processes, and the constants **a** = (a,b) now determine their amplitudes. For example, the first equation for the Hénon map says: take a line (e.g. y_i = constant, as a set of initial conditions) and stretch the middle of it vertically to make a parabola, with the amplitude of the stretch specified by the parameter a. The second equation says: squeeze the parabola by compressing the x-axis (by the factor b, where $b < 1$), to give y_{i+1} for the next iteration. Note that only two difference equations are needed to describe a system that required three differential equations. A periodic solution is given in this formulation by finding the values $\mathbf{x}^*$ for which $\mathbf{F}(\mathbf{x}_i,\mathbf{a}) - \mathbf{x}_i = \mathbf{0}$. As mentioned in the text, $\mathbf{x}^*$ is called a period one fixed point, because it corresponds to a single point on the map, and recurs each cycle. For the Hénon map this amounts to solving a quadratic for x^* to give

$$x^*_{1,2} = \frac{1}{2a}\left(-(1-b) \pm \left((1-b)^2 + 4a\right)^{1/2}\right), \quad y^* = bx^*_{1,2} \qquad (7)$$

Similarly, period n fixed points are found by $\mathbf{F}^{(n)}(\mathbf{x}_i,\mathbf{a}) - \mathbf{x}_i = \mathbf{0}$, where $\mathbf{F}^{(n)}$ represents n iterations of the mapping (i.e. $\mathbf{x}_{i+n} = \mathbf{F}(\mathbf{F}(\mathbf{F}(\ldots\mathbf{F}(\mathbf{x}_i,\mathbf{a})..)))$).

The stability of periodic solutions is much easier to compute using perturbation analysis with a set of difference equations than with a set of differential equations, and will be outlined here. In this case, $\mathbf{x}$ is written as $\mathbf{x}^* + \delta\mathbf{x}$, where the latter term represents a small perturbation from the periodic solution and the mapping is linearised around $\mathbf{x}^*$ to produce the matrix equation:

$$\delta\mathbf{x}_{i+1} = \underline{\mathbf{A}} \cdot \delta\mathbf{x}_i \tag{8}$$

where $\underline{\mathbf{A}}$ is defined for the two dimensional mapping in equation (6) by:

$$\mathbf{A} = \frac{\partial}{\partial \mathbf{x}_i}\mathbf{F}(\mathbf{x}_i, \mathbf{a})\bigg|_{\mathbf{x}=\mathbf{x}^*} = \begin{bmatrix} \left.\frac{\partial f}{\partial x_i}\right|_{\mathbf{x}=\mathbf{x}^*} & \left.\frac{\partial f}{\partial y_i}\right|_{\mathbf{x}=\mathbf{x}^*} \\ \left.\frac{\partial g}{\partial x_i}\right|_{\mathbf{x}=\mathbf{x}^*} & \left.\frac{\partial g}{\partial y_i}\right|_{\mathbf{x}=\mathbf{x}^*} \end{bmatrix} = \begin{bmatrix} -2ax^* & 1 \\ b & 0 \end{bmatrix} \text{ (for the Hénon map)} \tag{9}$$

Equation (8) is solved in the standard way by finding the eigenvalues ($s_{1,2}$) of $\underline{\mathbf{A}}$, which satisfy $\det(\underline{\mathbf{A}} - \underline{\mathbf{I}}s) = 0$ (where $\underline{\mathbf{I}}$ is the unit matrix). Labelling the corresponding eigenvectors $\mathbf{e}_{1,2}$, if the displacements from the fixed point along $\mathbf{e}_1$ and $\mathbf{e}_2$ respectively are δp and δq, then

$$\delta p_{i+1} = s_1 \delta p_i \text{ and } \delta q_{i+1} = s_2 \delta q_i \,. \tag{10}$$

If, say, $|s_1| < 1$, then the distance between $\mathbf{x}$ and $\mathbf{x}^*$ projected along the eigenvector $\mathbf{e}_1$ clearly decreases with each iteration. On the other hand, if $|s_1| > 1$ then this distance increases with each iteration. Close to the fixed point $\mathbf{x}^*$, the period between cycles $\Delta T \approx \Delta T^*$, where ΔT^* is the period of the fixed point. Hence equation (10) represents the periodic sampling of exponential behaviour with $s_{1,2} \approx \exp(\lambda_{1,2}\Delta T^*)$, where $\lambda_{1,2}$ are rates of exponential growth or decay, and correspond to the eigenvalues found by perturbation analysis of the differential equations describing the system. A stable fixed point is therefore indicated by $|s| < 1$ for both eigenvalues, and becomes unstable if $|s| > 1$ for any one of its eigenvalues. An unstable fixed point that gives rise to a UPO, being the result of a stretching process ($\mathrm{Re}(\lambda_+) > 0$) and a squeezing process ($\mathrm{Re}(\lambda_-) < 0$) as discussed in the previous section, therefore has $|s_-| < 1$ and $|s_+| > 1$. Noting that $-1 = \exp(i\pi)$, it is clear that a negative value of $s_{+,-}$ corresponds to $\mathrm{Im}(\lambda_{+,-}) = \omega_o/2$, where $\omega_o = 2\pi/\Delta T^*$, and indicates that the eigenvectors alternate their directions after each iteration.

For each fixed point of the Hénon map, the eigenvalues are given by:

$$s_{\pm} = -\left(ax^{*} \pm \left(a^{2}x^{*2} + b\right)^{1/2}\right) \tag{11}$$

Substituting the values of the fixed points into this equation, it is easy to show that x_1^* (corresponding to the fixed point with the negative second term in equation (7)) is always unstable ($|s_{+,-}| > 1$ for both eigenvalues, for all a and b). The other fixed point x_2^* always has $|s_-| < 1$, and has $|s_+| > 1$ only if $a > a_o = 3(1 - b)^2/4$. That is, this fixed point is stable when the stretching process is low in amplitude, and becomes unstable when the amplitude is increased above a threshold value. It is from this fixed point that a cascade of period doubling bifurcations ensue as a is further increased, leading to chaotic behaviour as described earlier.

Unstable Periodic Orbits and the Return Map

As mentioned earlier, an unstable periodic orbit occurs when the state of the dynamical system approaches an unstable fixed point because of the squeezing process (described by $|s_-| < 1$) and diverges because of the stretching process (described by $|s_+| > 1$). We now examine how a UPO due to an unstable period 1 fixed point appears on the first return map of a single variable x. Consider the local region surrounding the fixed point $\mathbf{x}^*$ where the linear approximation of the mapping function described above is valid. Within this region, the consecutive points of the UPO in (x,y) space mark out a hyperbolic path that asymptotes along the direction of approach , given by the eigenvector **e**, and the direction of divergence, given by $\mathbf{e}_+$. Both of these eigenvectors have components in the direction of the variable x, hence δx may be written as $\delta x_i = \alpha\delta q_i + \beta\delta p_i$ (where α and β are constants), where each iteration decreases δq_i by the factor s_-, and increases δp_i by the factor s_+. Writing $\beta q_i / \alpha p_i = k_i$, it is easy to show that the one dimensional mapping from δx_i to δx_{i+1} may be written as

$$\delta x_{i+1} = s_{+}\delta x_i \frac{1 + k_i\left(s_{-}/s_{+}\right)}{1 + k_i} \tag{12}$$

During the approach phase of the UPO, initially $k_i >> 1$, and equation (12) reduces to:

$$\delta x_{i+1} \approx s_{-}\delta x_i \tag{13}$$

Each iteration decreases k_i by the factor (s_-/s_+), making the above approximation invalid as k_i approaches 1, and the UPO enters the departure phase. Further iterations, for which $k_i << 1$, may be approximated by

$$\delta x_{i+1} \approx s_{+}\delta x_i \tag{14}$$

This result allows UPOs to be identified on the first return map of x, by searching for sets of consecutive points that describe these two straight lines surrounding the fixed point value, with the slopes s_- and s_+ during the approach and departure phases respectively.

We should also consider how this result affects the period of time ΔT_i between x_i and x_{i+1}, since we use a return map of ΔT's to find UPOs, as described in Section 2.2 of this paper. If $\mathbf{x}_i$ is close to $\mathbf{x}^*$ such that the variations in x_i are described by a linear system, then ΔT_i will also be close to the period of the fixed point ΔT^* and hence will also be subject to the same linear behaviour. This allows UPOs to be found in the sequence ΔT's.

Appendix B

Figure B. 1 shows the distributions of a number of parameters characterising each of the UPO candidates that were binned to investigate whether their distributions varied significantly from that of the fake UPOs found in the surrogate sets. The effect on the distributions of the filtering process, discussed in Section 2.5 of the text, and the distributions of the candidates and surrogates that were rejected by the filter are shown in the second and third rows of the figure.

References

[1] Bak P. E., Yoshino R., Asakura N., Nakano T., 1999 Phys. Rev. Lett. **83** 1339

[2] Wagner F. *et al.* 1982 Phys. Rev. Lett. **49** 1408

[3] The ASDEX Team, 1989 Nucl. Fusion **29** 1959

[4] Gohill P. *et al.* 1988 Phys. Rev. Lett. **61** 1603

[5] Zohm H. 1996 Plasma Phys. Control. Fusion **38** 105

[6] Suttrop W. 2000 Plasma Phys. Control. Fusion **42** A1

[7] Hofmann F. *et al.* 1994 Plasma Phys. Control. Fusion **36** B277

[8] Weisen H. *et al.* 1995 Plasma Phys. Control. Fusion **38** 1137

[9] Martin Y. To be submitted to Nuclear Fusion.

[10] Dutch M. J. *et al.* 1995 Nuclear Fusion **35** 650

[11] Bak P. E., 1997 PhD Thesis, University of London

[12] Conner J. W., 1998 Plasma Phys. Control. Fusion **40** 191

[13] Martien P., Pope S. C., Scott P. L., Shaw R. S., 1985 Phys. Lett A **110** 399; Flepp L., Holzner R., Brun E., 1991 Phys. Rev. Lett. **67** 2244; Lathrop D. P., Kostelich E. J. 1989 Phys Rev. A **40** 4028.

[14] Dolan K., Witt A., Spano M. L., Neiman A. Moss F., 1999 Phys. Review E **59** 5235

[15] Taylor J. R. 1982 *An Introduction to Error Analysis*, Oxford University Press

[16] Degeling A. W., Martin Y. R., Bak P. E., Lister J. B., X. Llobett, 2001 Dynamics of Edge Localised Modes in the TCV tokamak, CRPP, Lausanne preprint LRP (699/01).

[17] Gilmore R. 1998 Rev. Mod. Phys. **70** 1455.

[18] Ott E., Greborgi C., Yorke J. A., 1990 Phys. Rev. Lett. **64** 1196

[19] Lichtenberg. A, Lieberman M. A., 1983 *Regular and Stochastic Motion*, Springer-Verlag

[20] Pierre, Tu N. V., 1992 *Dynamical Systems An Introduction with Applications in Economics and Biology 2nd Ed.* Springer-Verlag Berlin

[21] Morrison F., 1991 *The Art of Modelling Dynamical Systems* Wiley, New York

[22] Beltrami E. 1987 *Mathematics for Dynamical Modelling*, Academic Press, San Diego

[23] Rössler O. E., 1976 Phys. Lett. **57a** 397

Figures

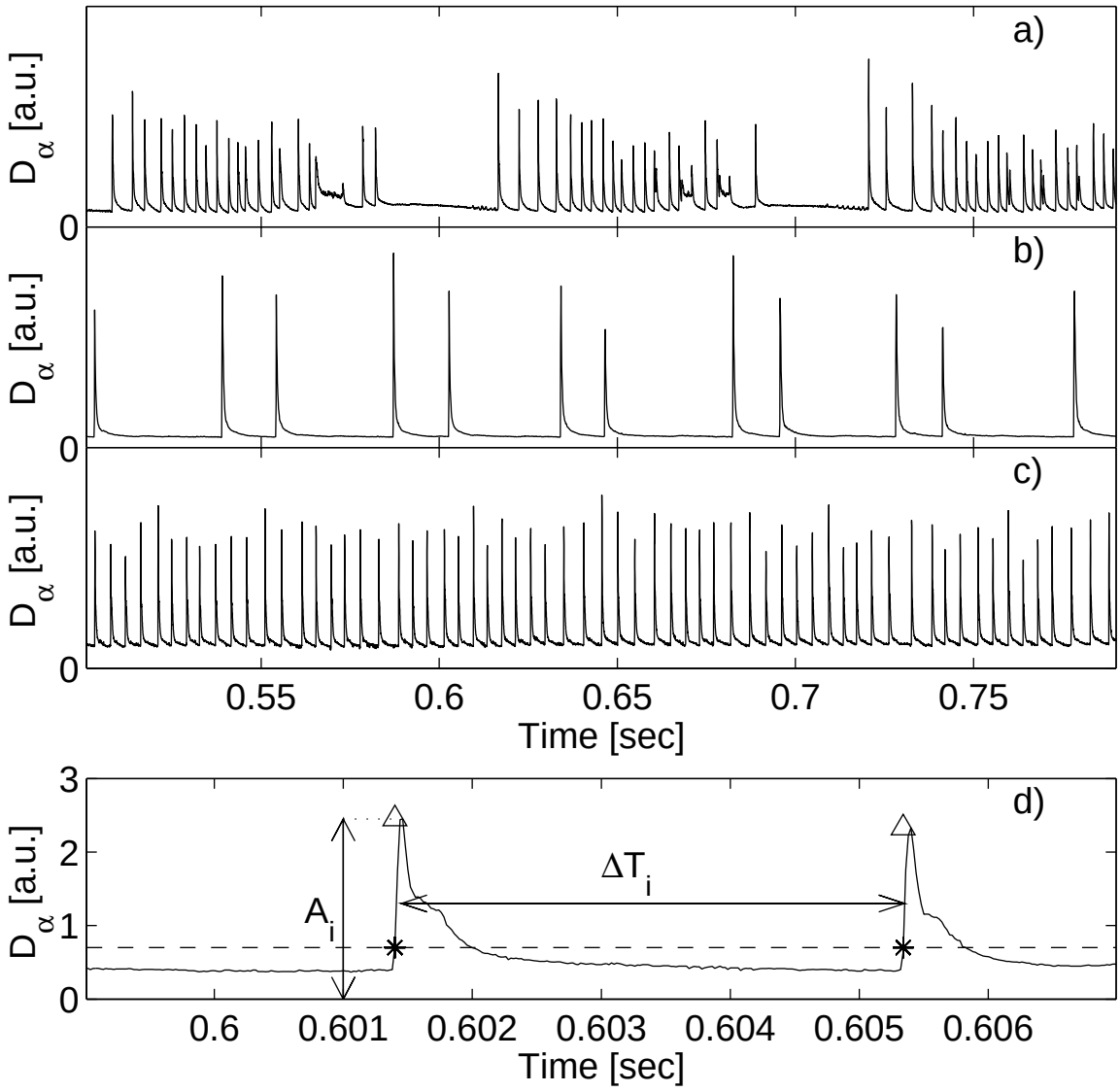

Figure 1: D_α emission as a function of time showing three typical ELMy H-modes with widely varying dynamics : a) Intermittent bursts of ELMs and ELM-free periods ; b)Regular period two (long – short – long – short) ELMs ; c) A steady ELMy H-mode showing fluctuating ELM periods and amplitudes ; d) An expanded view of (c) showing the definitions for ELM amplitude (A_i) and the inter-ELM period (ΔT_i) based on a threshold detection scheme.

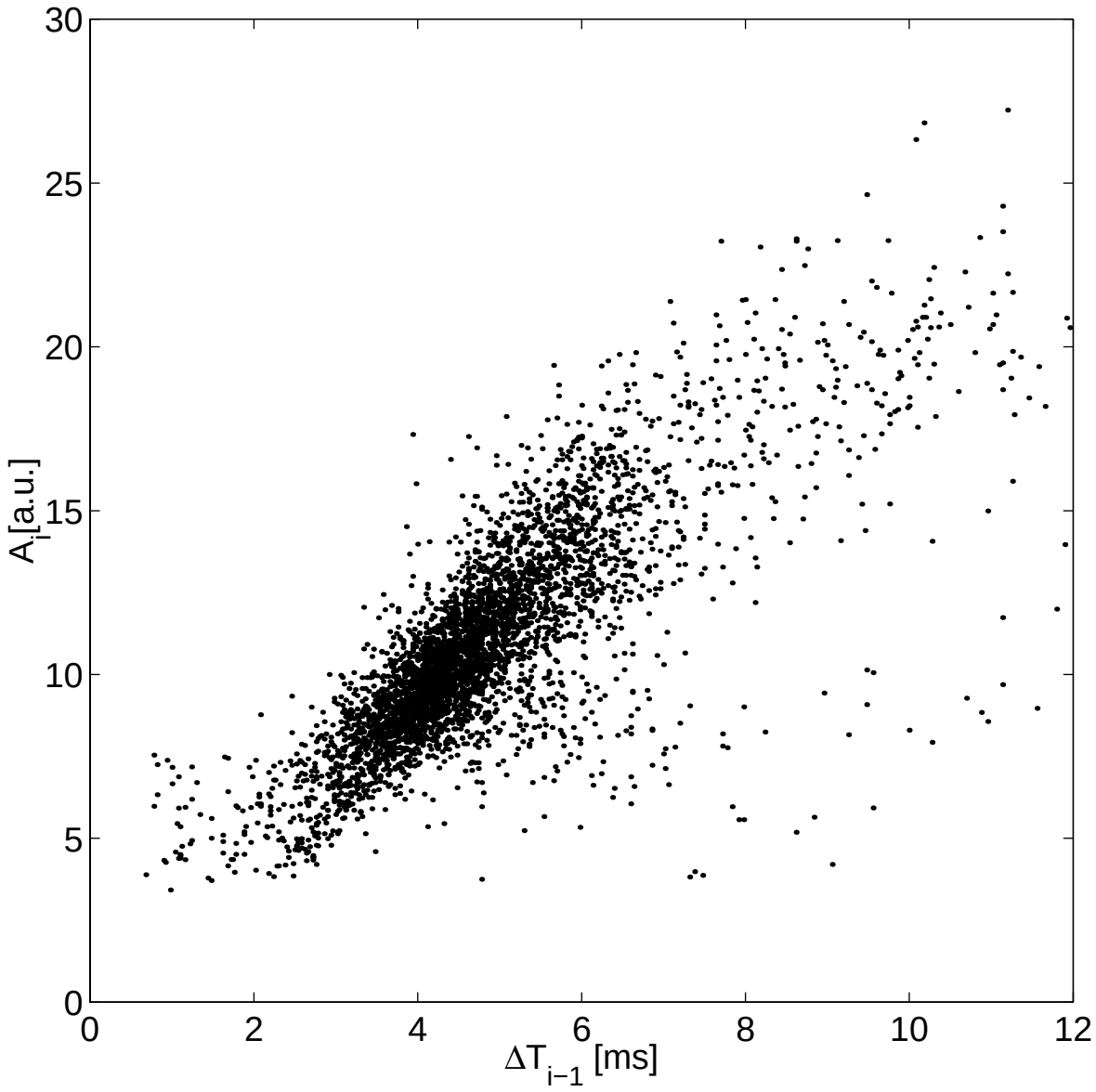

Figure 2: ELM amplitude (A_i) versus the preceding inter-ELM period (ΔT_{i-1}). Note in particular that no large ELMs are found following a short ELM period.

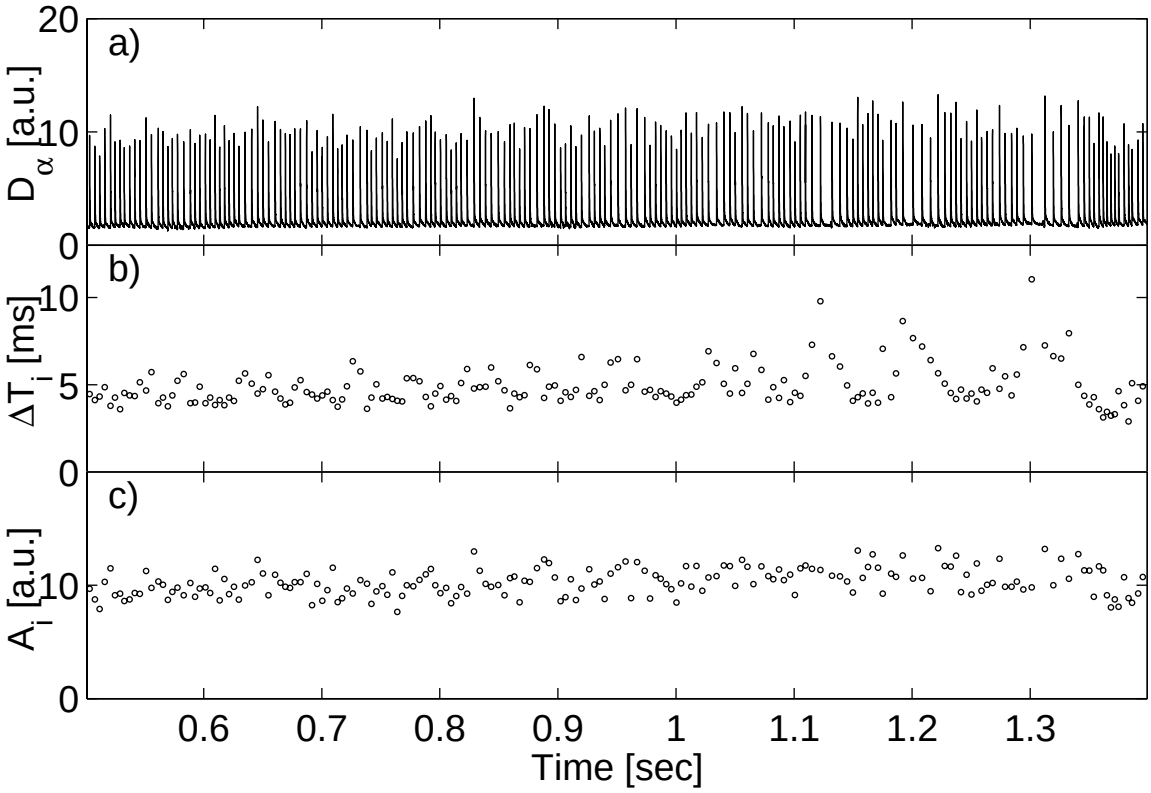

Figure 3: a) D_α time-series showing a series of ELMs ; b) The inter-ELM period discrete time series ΔT_i versus t_i; c) The ELM amplitude discrete time series A_i versus t_i.

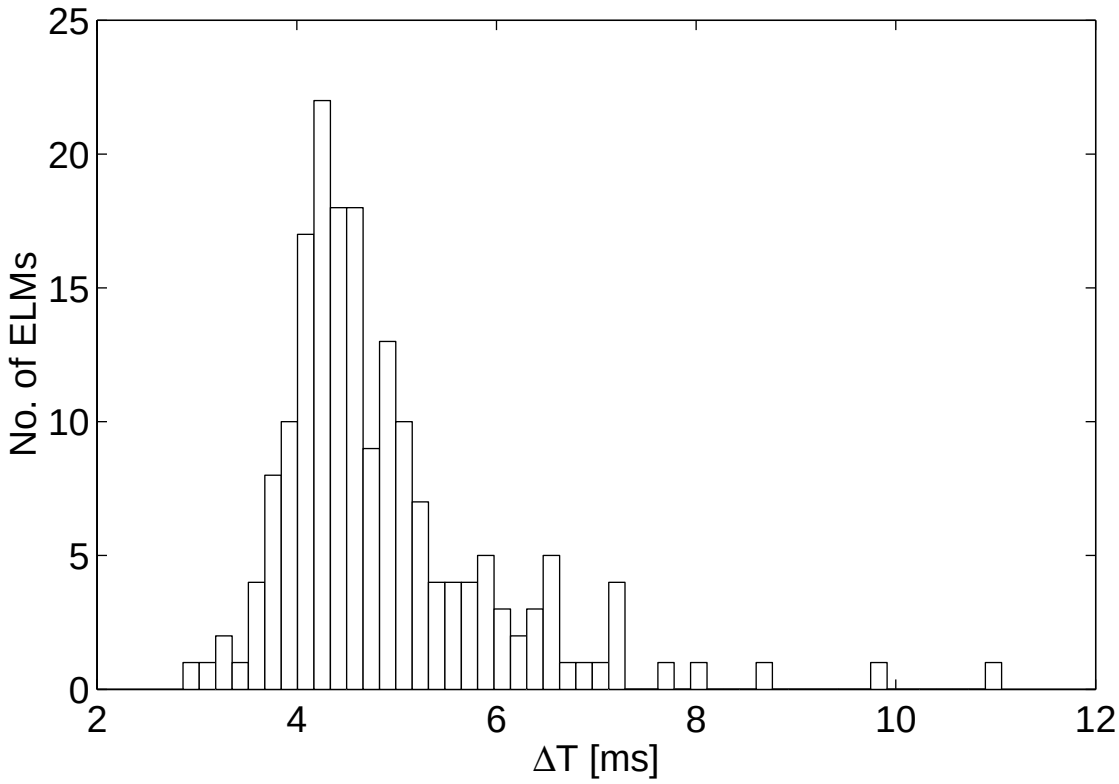

Figure 4: A histogram of the number of ELMs as a function of the inter-ELM period.

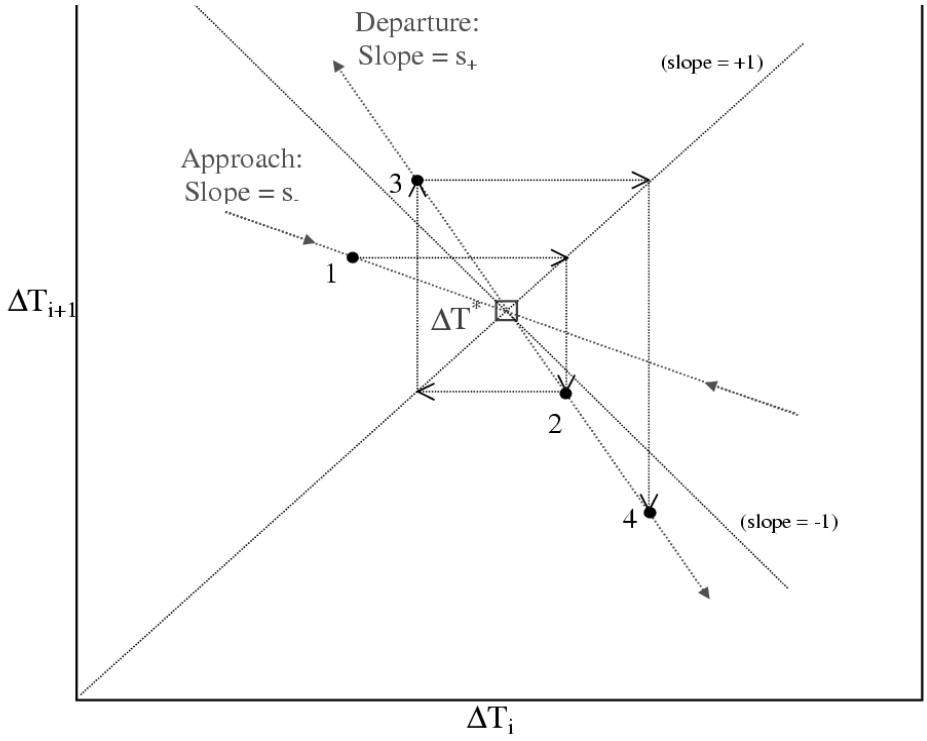

Figure 5: Schematic diagram of a UPO on the first return map. Dotted lines indicate the slope of approach and departure, and the order of consecutive points (solid dots) are numbered, and connected by horizontal and vertical arrows (indicating the process of iteration from ΔT_i to ΔT_{i+1}). The fixed point ΔT^* occurs at the common intersection of the lines of approach and departure with the diagonal. Dotted lines with slopes +1 and –1 are also shown.

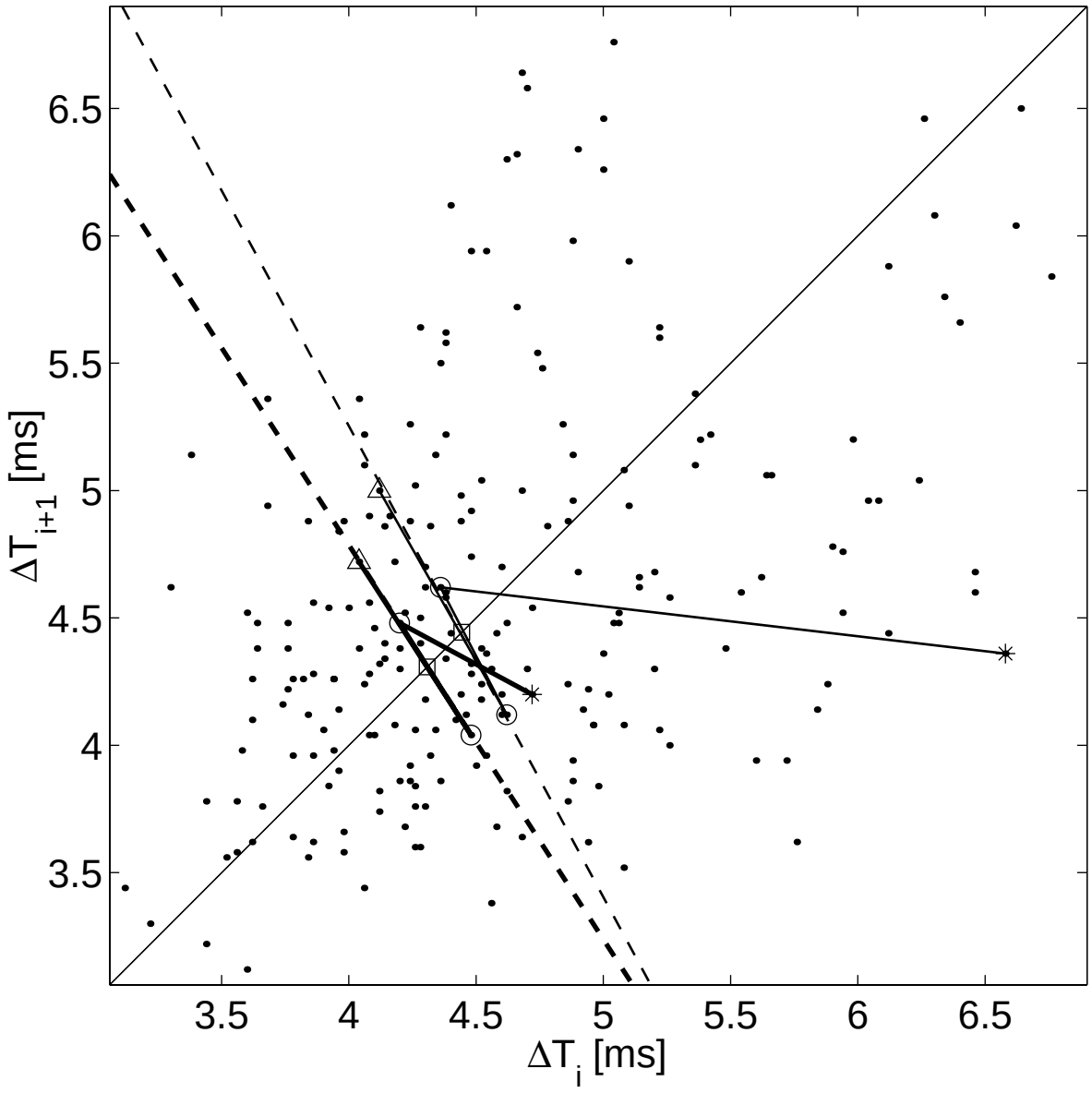

Figure 6 : The first return map of the inter-ELM periods ΔT_i versus ΔT_{i+1} for a single discharge. Two UPOs are shown on this figure (each set of points connected by solid lines). The first point in each sequence is marked by '*', the middle points by 'o' and the last point by 'Δ'. The slopes of the dashed lines are calculated from the exponential growth rate of the UPO points from the fixed point in the time-series data, as shown in Figure 7.

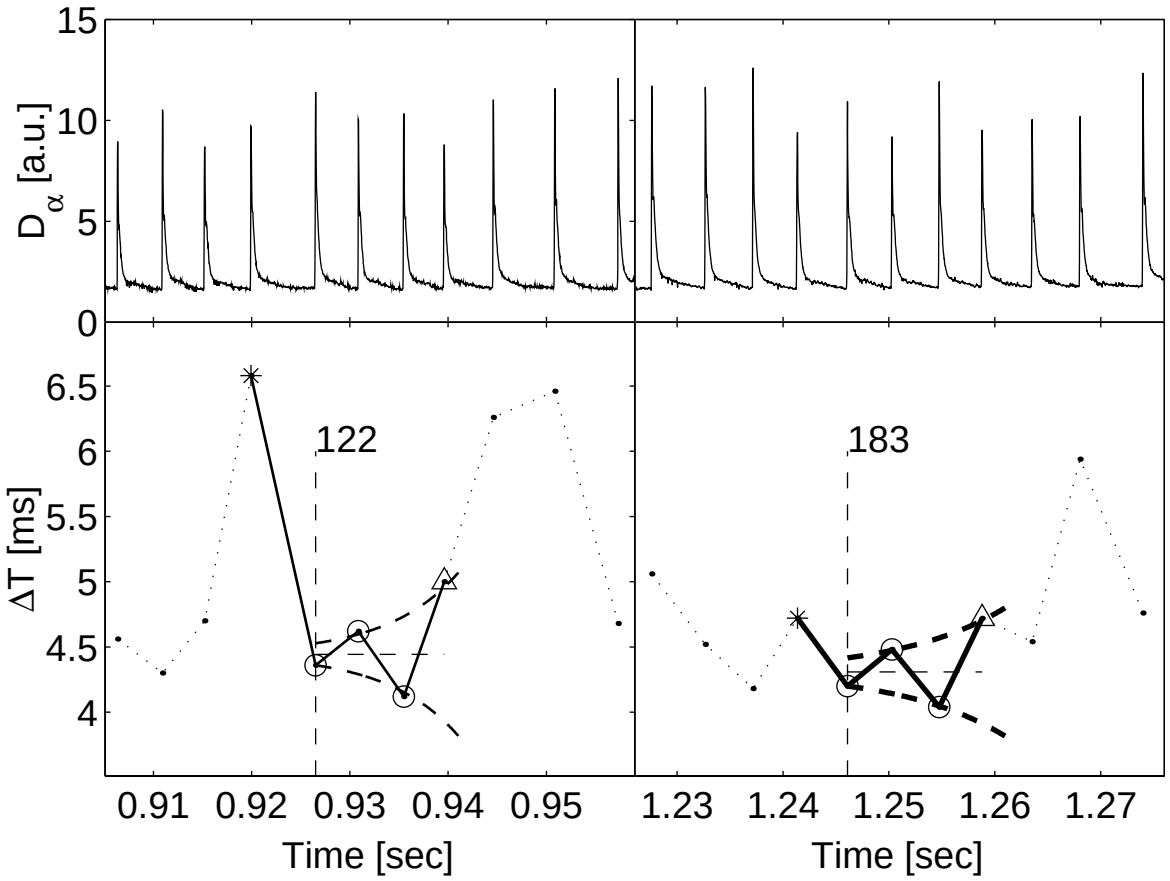

Figure 7: The top left and right plots show the D_α signal of the ELMs that comprise the UPOs shown in Figure 6. The bottom left and right plots show the corresponding time series of inter-ELM periods, with dashed lines indicating : the onset of the departure phase of the UPO (veritical line), the value of the fixed point (horizontal line), and the fitted exponentials for each sequence. The symbols for the UPO points are the same as in Figure 6.

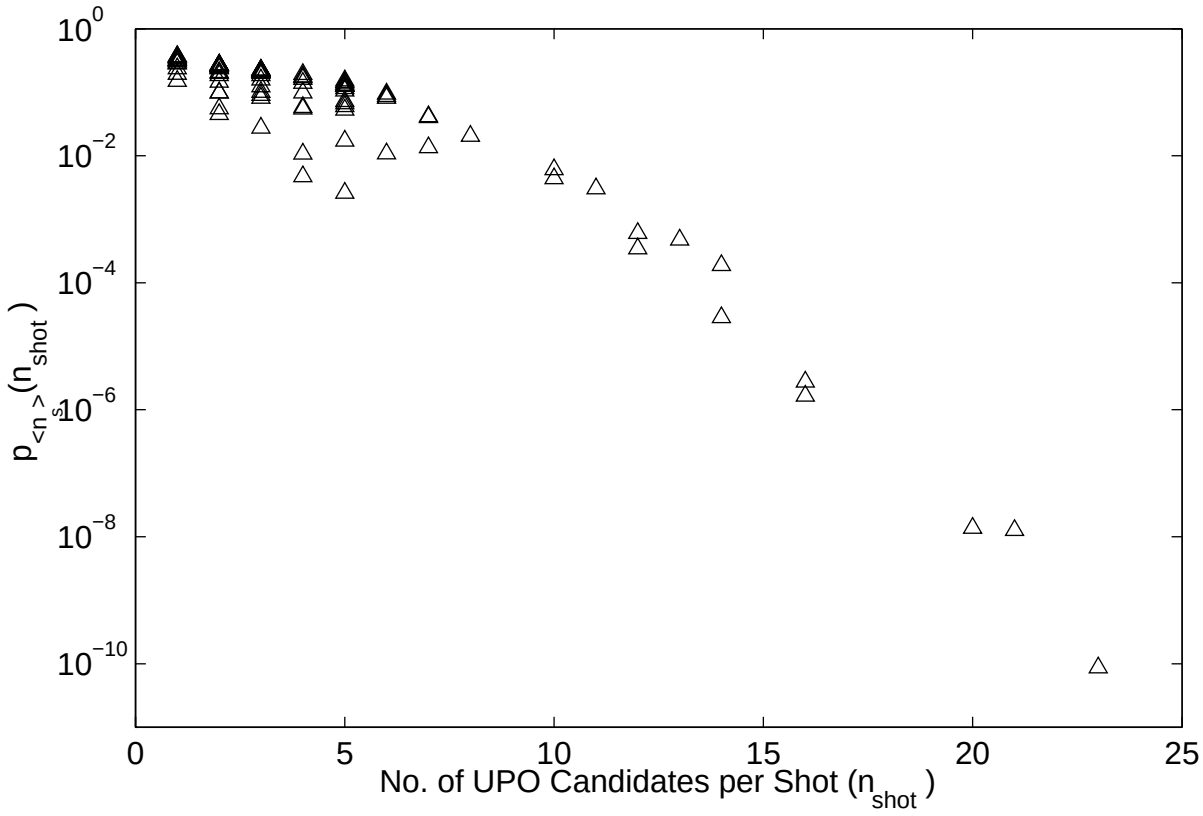

Figure 8: The probability $p_{\langle n_s \rangle}(n_{shot})$ that the number of UPO candidates found in each discharge (n_{shot}) is the result of a random process obeying Poisson statistics with a mean value $\langle n_s \rangle$, given by the mean number of fake UPOs found in the surrogates corresponding to each discharge.

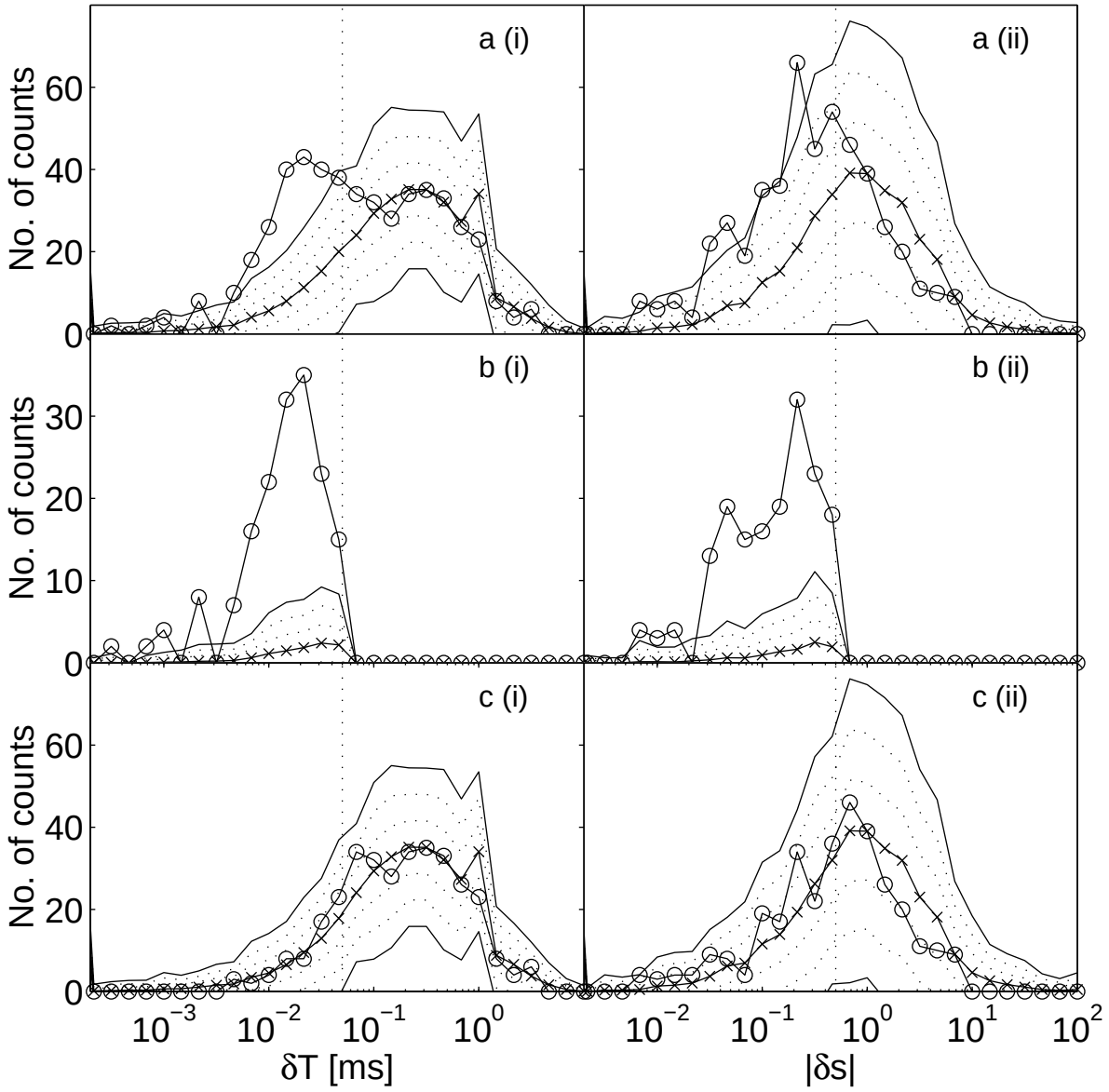

Figure 9: (i) and (ii) : The respective distributions summed over all discharges of δT and δs for the UPO candidates in the experiment data (solid line with 'o' symbols), compared with the distributions for the mean values of the surrogate sets (solid line with 'x' symbols). The solid lines with no symbols indicate the mean of the surrogate distributions ± 3 standard deviations in each case (each standard deviation is indicated by a dotted line). a): The distributions for the raw data. b) : The filtered data, resulting from the removal of all points to the right of the vertical dotted line in each plot (the upper threshold values of the filter). Note that the surrogates are subject to the same filter, and that the surrogates of any discharge that has no surviving points are also removed. c) : The distribution produced by the negation of this filter i.e. the distribution of points from the experimental data and surrogate sets that were rejected by the filter.

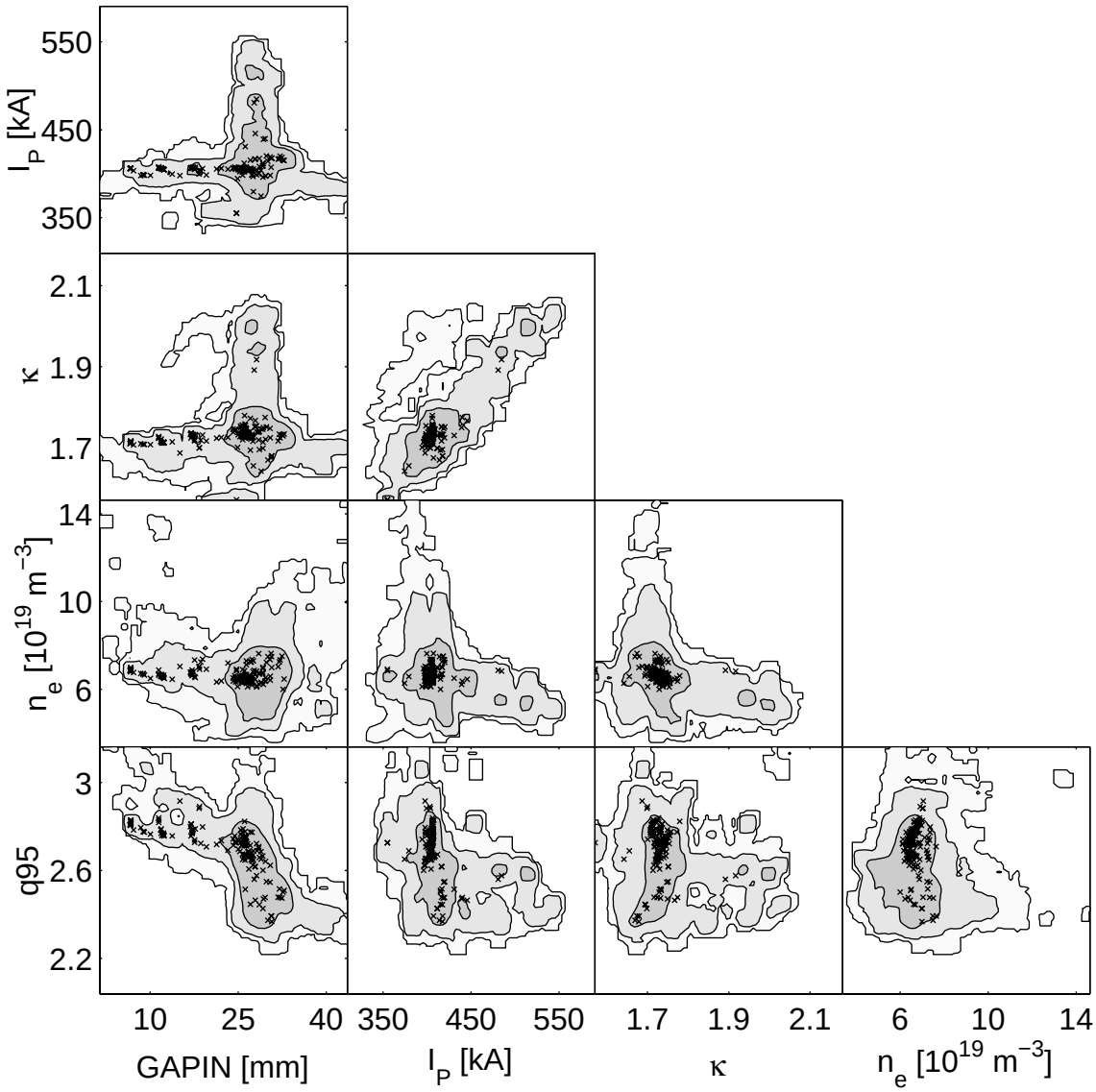

Figure 10: Filled contours represent the total amount of time spent in the ELMy H-mode (over all discharges) in each of the 80x80 bins of the parameter space shown in each plot, spaced at 1, 10 and 100 ms per bin (light, medium and dark grey levels respectively). All combinations of the parameters [I_P, κ, n_e, Δ_{in} and q_{95}] are shown. The small black crosses indicate the position in parameter space corresponding to each UPO, hence the density of these crosses compared with the filled contour levels indicates the frequency of occurrence of UPOs in these projections of parameter space.

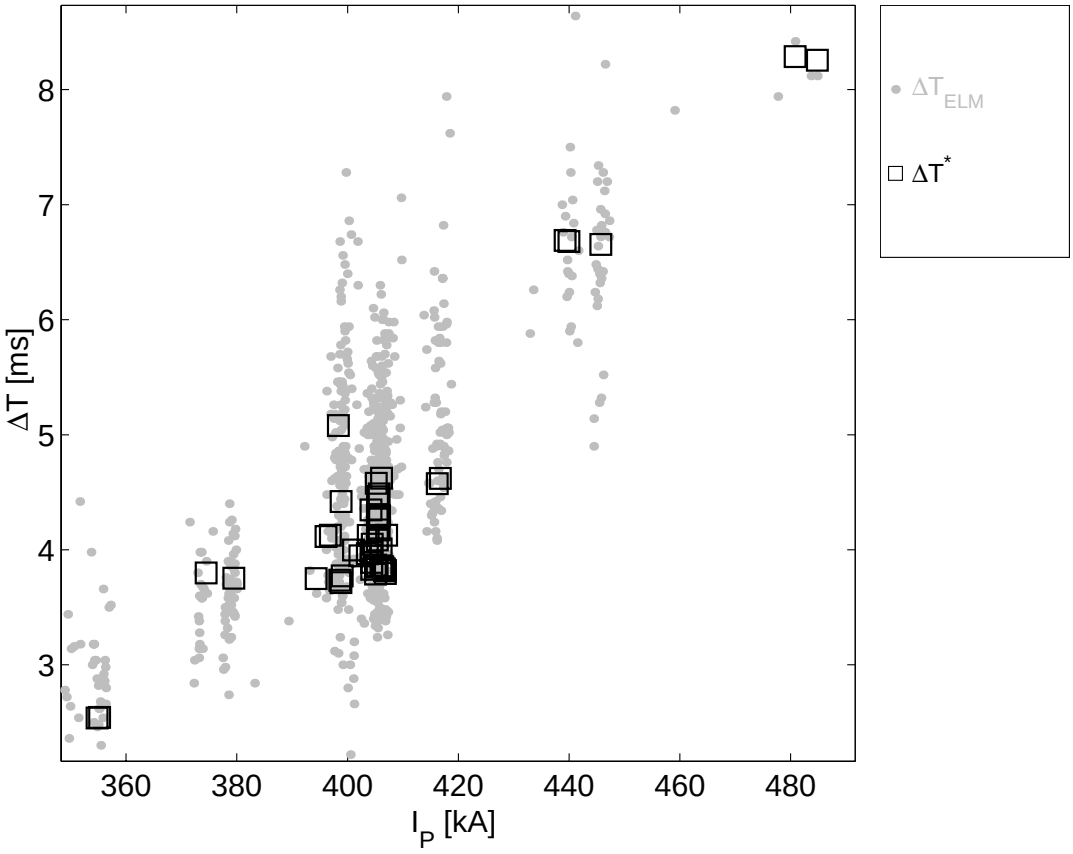

Figure 11 : Variation of ΔT^* with I_P for UPOs with plasma parameter values within the window given in Table 2. The grey points are samples of the inter-ELM period that passed the same parameter window.

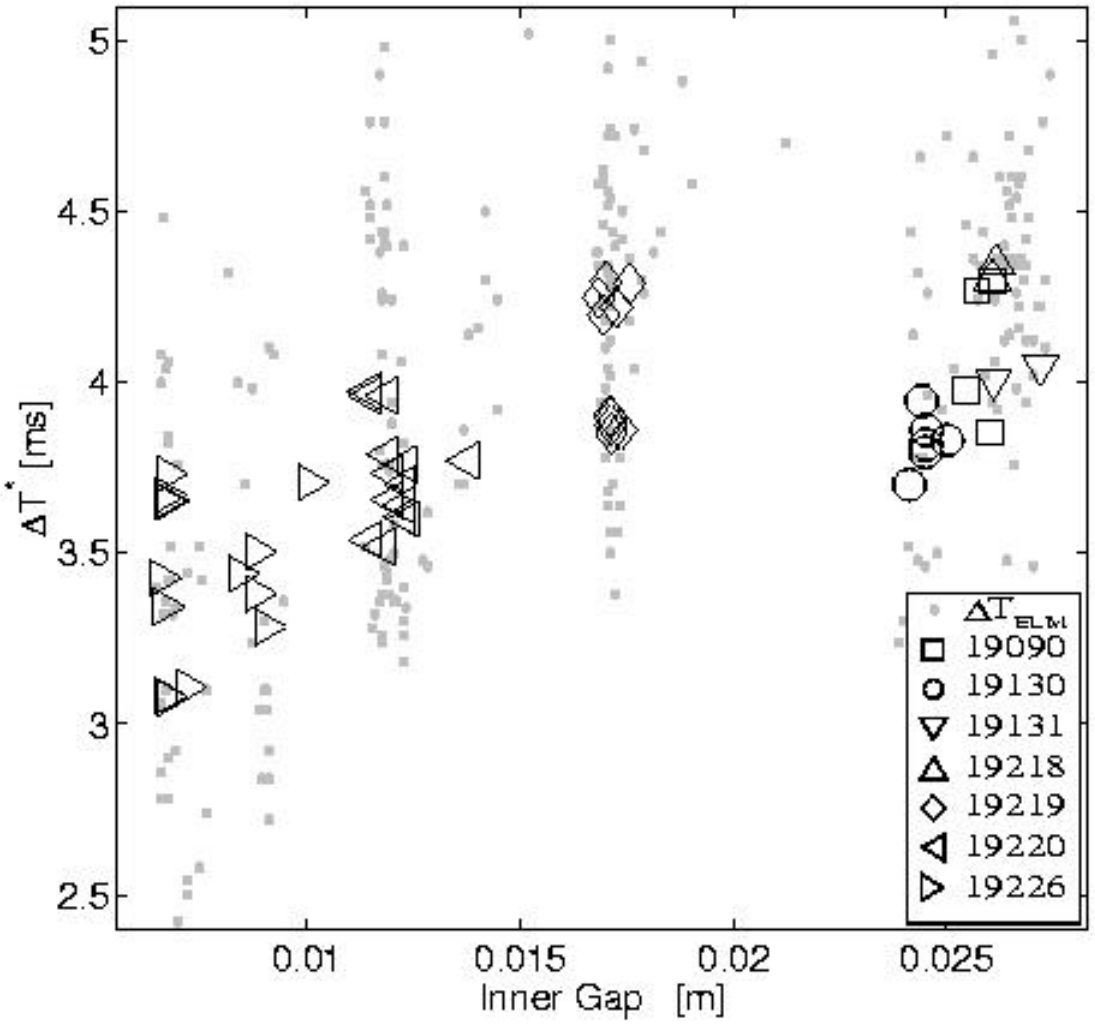

Figure 12: Variation of ΔT^* with Δ_{in} for UPOs with plasma parameter values within the window given in Table 2.The symbols indicate the discharge number corresponding to each UPO. The grey points are samples of the inter-ELM period that passed the same parameter window.

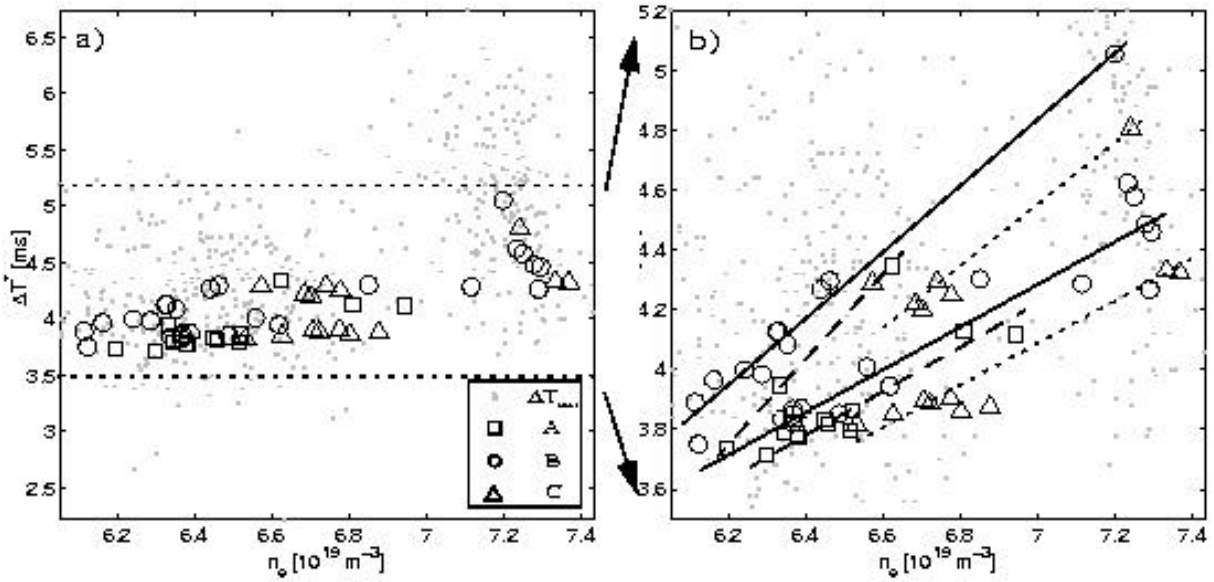

Figure 13: a) Variation of ΔT^* with n_e for 3 groups of UPOs (A, B and C) with plasma parameter values within the windows given in Table 2. The grey points are samples of the inter-ELM period that passed the same parameter window. b) The same figure with increased y-axis scale, showing possible separations into upper and lower trends in each group.

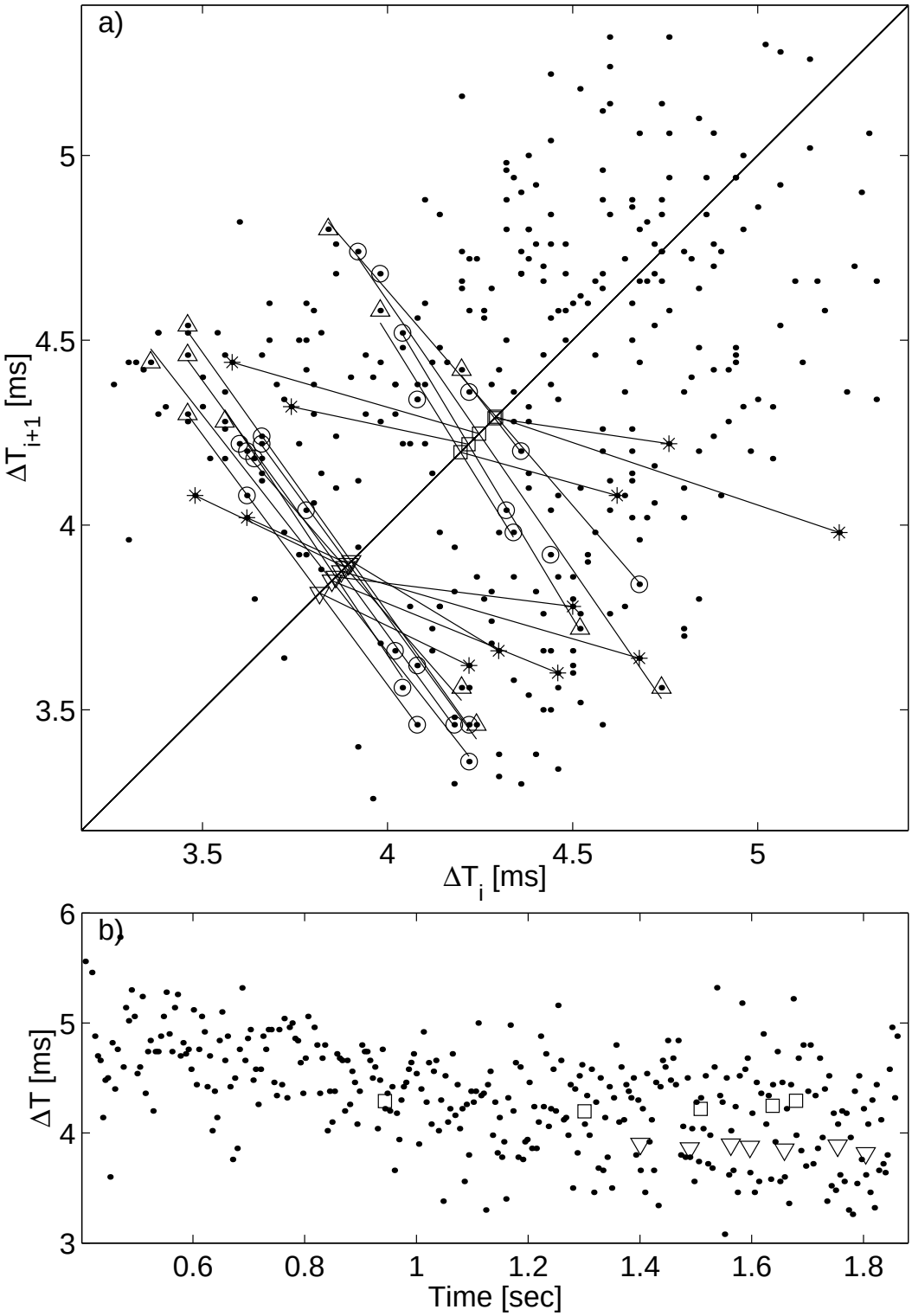

Figure 14 : a) The 1st return map of ELM periods for discharge 19219, showing two distinct groupings of UPOs (fixed points designated by ∇ and □ in each group). b) The time series of ΔT's for this discharge. Also shown are the occurrence time of UPOs, and their corresponding ΔT^* values, with □ and ∇ designating an upper and lower group of values respectively.

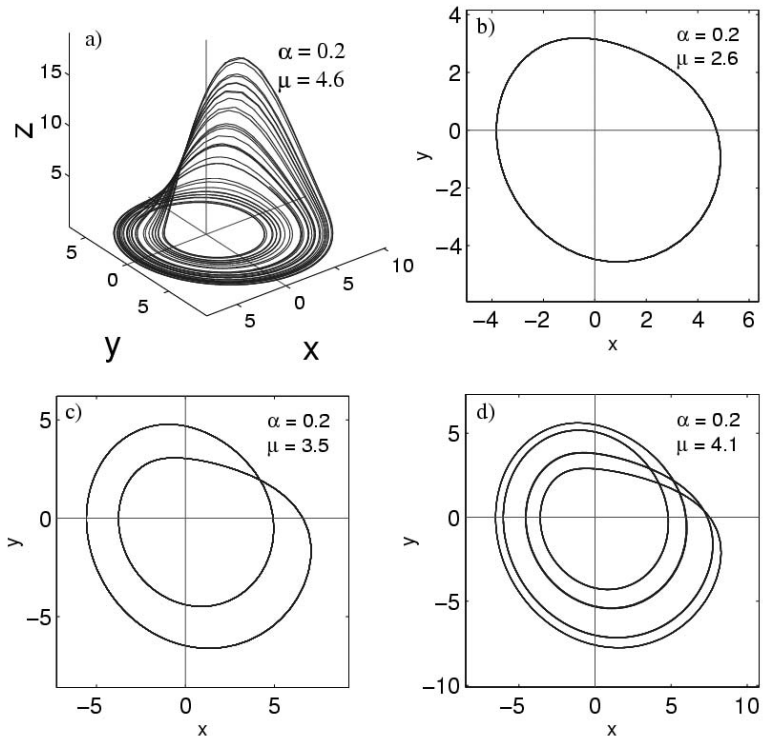

Figure A.1: a) The Rössler dynamical system in a chaotic state. b – d) Periodic (i.e. non-chaotic) solutions for the Rossler dynamical system projected onto the x – y plane, showing period doubling bifurcations (values of α and μ shown in each figure).

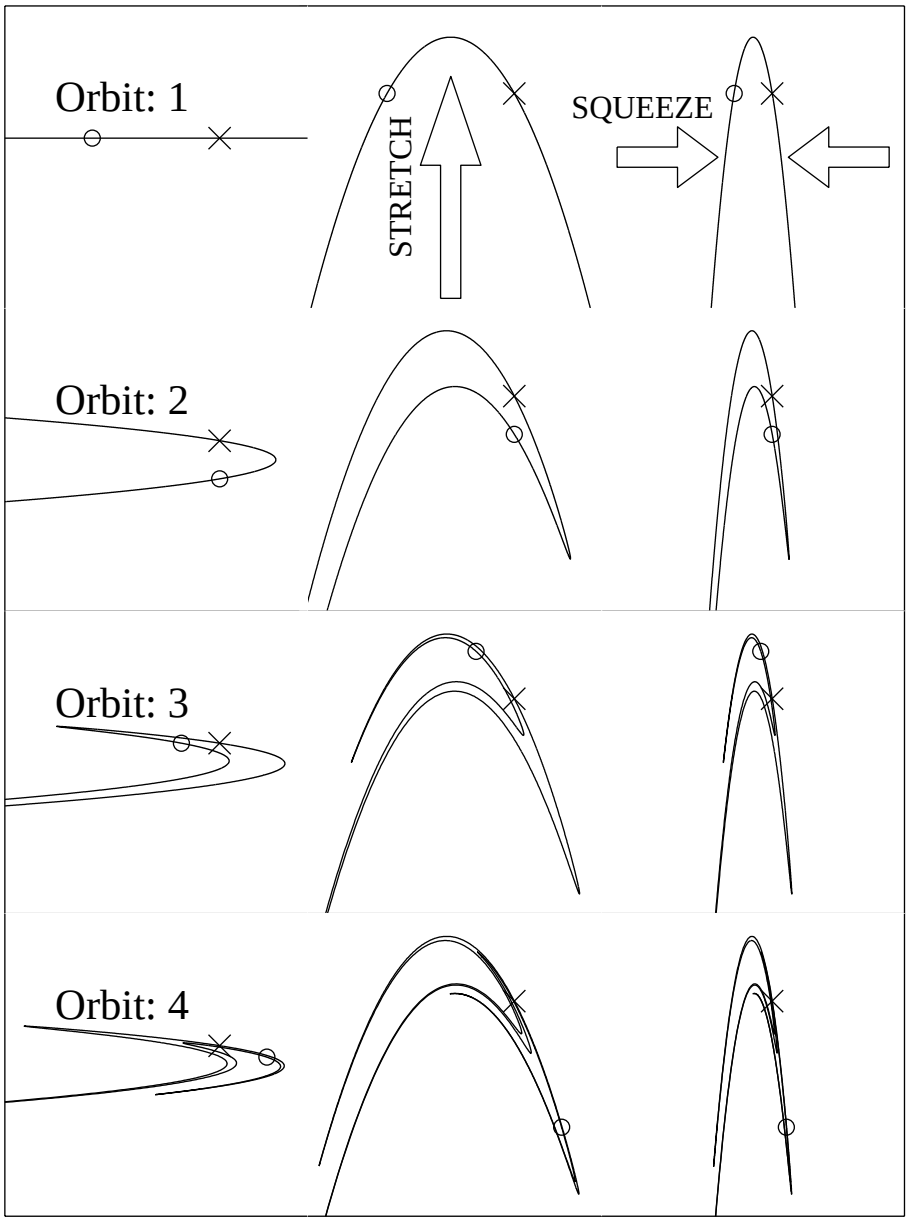

Figure A.2 : An illustration of the periodic stretching and squeezing processes that give rise to the Rössler attractor, with the squeezing process kept weak to visualise the build up of a fractal structure of leaves. Each diagram along a row (labelled orbit 1 – 4) represents a cross section of the attractor at three different points of an orbit, with the next orbit starting on the row below. The x in each diagram represents an unstable fixed point, and the circle is a UPO trajectory that first approaches, then diverges from the orbit. Note the alternation of the trajectory above and below the unstable fixed point. This diagram is produced using the Hénon mapping equations (6), with a = 1.4 and b = 0.3, by starting with $y_1 = y^*$ and $\{x_1: -3 < x_1 < 3\}$, and iterating 3 times.

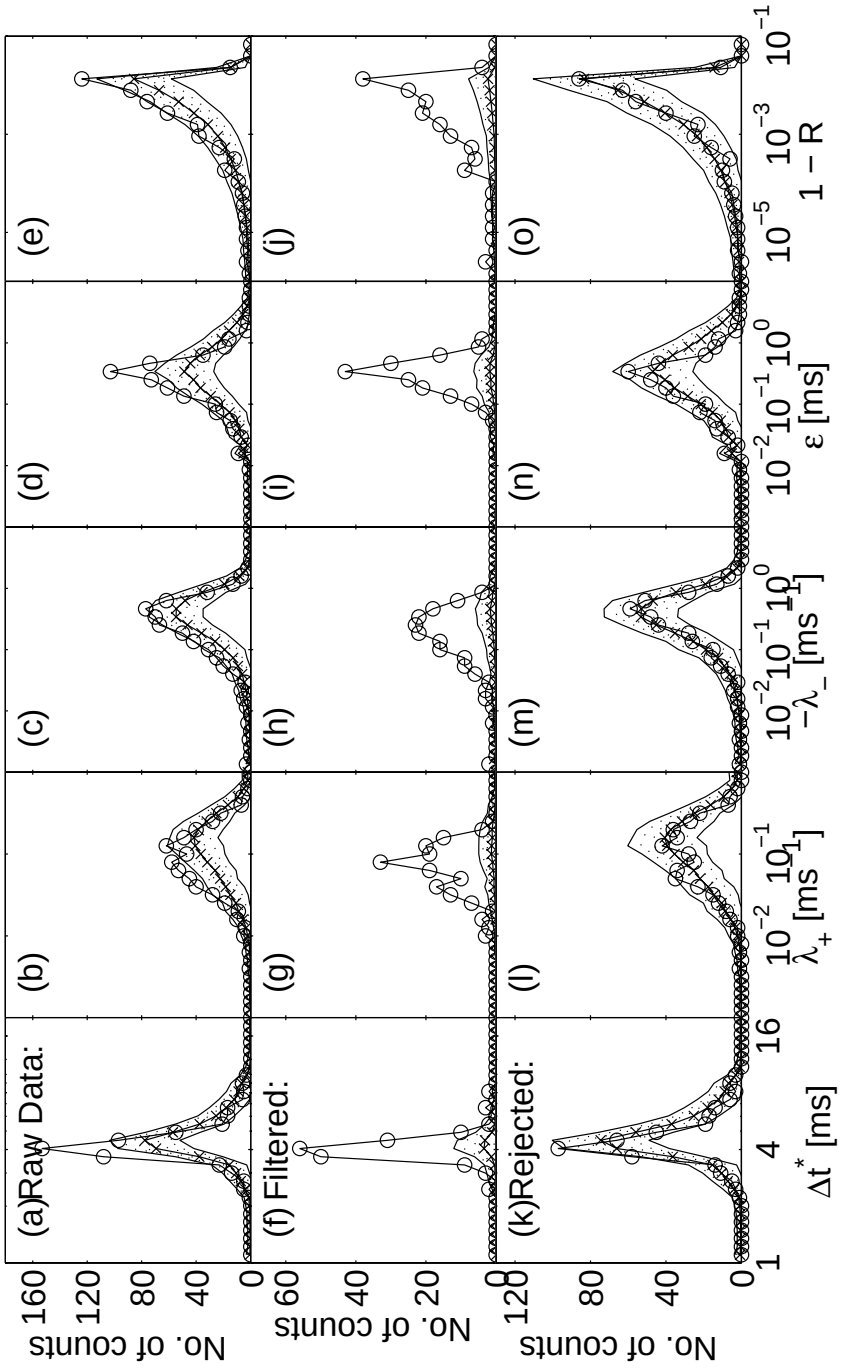

Figure B. 1 The distributions of UPO candidate properties summed over all discharges for the experiment data and the surrogate sets, binned logarithmically. The line definitions are the same as Figure 9. From left to right the UPO parameters are : the unstable fixed point periodicity (ΔT^*) ; exponential growth rate (λ_+) ; (-1×) exponential decay rate (λ) ; point of closest approach to ΔT^* (ε) ; (1 -) the linear correlation coefficient for the departure phase of the UPO (R). As in Figure 9, the top row of figures (a – e) shows the raw data, the second row (f – j) shows the data after filtering, and the third row (k – o) shows data rejected by the filter.